Fall 11-23-2016

Investigation of Jet Dynamics in Cross-Flow: Quantifying Volcanic Plume Behavior

Graham Freedland
Portland State University

Investigation of Jet Dynamics in Cross-Flow: Quantifying Volcanic Plume Behavior

by

Graham Freedland

A thesis submitted in partial fulfillment of the
requirements for the degree of

Master of Science
in
Mechanical Engineering

Thesis Committee:
Raúl Cal, Chair
Gerald Recktenwald
Derek Tretheway

Portland State University
2016

Abstract

Volcanic eruption columns inject high concentrations of ash into the atmosphere. Some of this ash is carried downwind forming ash clouds in the atmosphere that are hazardous for private and commercial aviation. Current models rely on inputs such as plume height, duration, eruption rate, and meteorological wind fields. Eruption rate is estimated from plume height using relations that depend on the rate of air entrainment into the plume, which is not well quantified. A wind tunnel experiment has been designed to investigate these models by injecting a vertical air jet into a cross-flow. The ratio of the cross-flow and jet velocities is varied to simulate a weak plume, and flow response is measured using particle image velocimetry. The plumes are characterized and flow data relative to the centerline is examined to measure the growth of weak plumes and the entrainment velocity along its trajectory. It was found that cross-flow recirculates behind the jet and entrainment occurs both up and downstream of the jet. Analysis of the generation of turbulence enhanced results by identifying the transition point to bending plume and the growth of the shear layer in a bending plume. This provides information that can be used to improve models of volcanic ash concentration changes in the atmosphere.

Acknowledgements

The author would like to thank Dr. Raúl Cal for guidance through the Masters program, Portland State University's Department of Mechanical and Materials Engineering for funding and support, the members of the Wind Energy and Turbulence Lab including Dr. Nicholas Hamilton and Elizabeth Camp for training and guidance through experiments, Dr. Steven Solovitz from Washington State University and Dr. Larry Mastin of USGS for guidance through this project, Joshua McCraney for coding and mathematical theory support, as well as Dr. Mark Glauser and Dr. Jacques Lewalle from Syracuse University for guidance during my early research experiences as an undergraduate at Syracuse University.

Contents

List of Tables

List of Figures

Nomenclature

α	Perpendicular entrainment coefficient
β	Bent plume entrainment coefficient
D	Diameter of the jet exit
g	Gravitational acceleration
k	Turbulent kinetic energy
l_b	Buoyancy length scale
L^*	Non-dimensional length of the plume
$\hat{m}$	Slope of the jet centerline
ρ_p	Density of the plume
ρ_0	Ambient air density
R_v	Jet to free-stream velocity ratio
S_{CL}	Streamwise trajectory of the plume
v_e	Entrainment velocity
v_{jet}	Velocity of the jet
v_{in}	Inflow velocity
$V_{\parallel}$	Flow parallel to a line
$V_{\perp}$	Flow perpendicular to a line
x^*	Non-dimensional axial dimension defined as x/D
$x^*_{\perp}$	Perpendicular distance in diameters off the centerline
y^*	Non-dimensional vertical dimension defined as y/D
y^*_t	Diameters above jet exit for transition to bending regime

Chapter 1

Introduction and Motivation

Since the eruption of Eyjafjallajökull, a volcano in Iceland, shut down the majority of European airspace in 2011, the development of a more precise model for volcanic plume development became a major subject of research within the scientific community. After models over-predicted the reach of critically dense ash clouds, it became clear our fundamental understanding of plumes was incomplete.

The development of eruption models to predict development and movement of ash clouds is commonly compared to historical volcanic eruptions (see Mastin et al. [15], Bonadonna et al. [2, 3], Briggs [5]). The models were found to contain a large level of uncertainty [24], which was found to be a closure argument known as entrainment. As a volcano ejects ash into the atmosphere, the ambient air mixes with the plume to achieve one of two states. The first case, known as a Plinian column, occurs when the concentration of ash decreases and the plume density drops below that of the ambient air, becoming positively buoyant before its upward momentum drops below zero [21]. The second is the opposite effect, where the plume does not achieve positive buoyancy and rains back down to earth as a pyroclastic flow [21]. While both plume studies present viable opportunities for investigation, the large scale development of Plinian columns has become the focus of volcanic models.

Positively buoyant plumes can be divided into three sections: strong plume, bending plume and bent plume [4] as shown in Figure 1.1. When the eruption rate (or ejection speed) far exceeds the cross-wind speed, the ash rises until the density reaches a neutrally buoyant point; alternatively the shear layer slows down the plume until cross-flow dominates. The second case is known as a weak plume and will be the focus of this investigation. Examining the characteristics of this type of flow led to the development of the Taylor entrainment approximation first proposed by Taylor [23] and revised by Morton et al. [16].

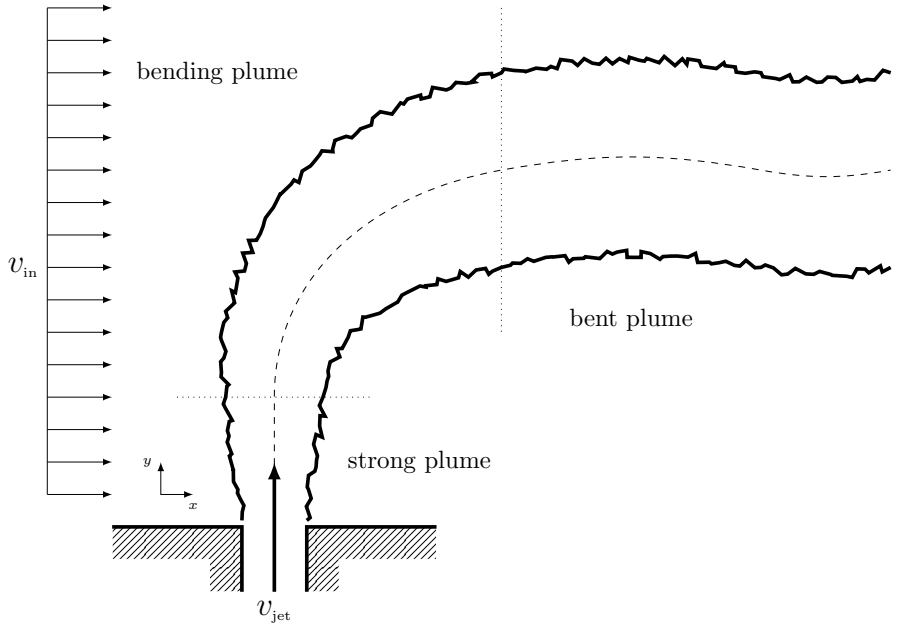

Figure 1.1: Sections of a buoyant plume from a jet

The Taylor entrainment approximation comes from the examination of the shear layer of the plume and the ambient air where, at the boundary, ambient air is being pulled into and mixes with the plume. The entrainment coefficient, α, is the closure argument that has been studied thoroughly to improve models of strong plumes, both

horizontal [12], and vertical, identified as the ratio of entrained air to exit velocity. For vertical jets, one experiment on a using micromanometers found that the best fit was an entrainment coefficient of $\alpha = 0.08$, [9, 19] while a PIV experiment found this value to be $\alpha = 0.03$. [20] Experimentally, the entrainment of a vertical jet of air has been determined with improved accuracy, but cannot be used for all models of plumes. When evaluating a weak plume, the entrainment becomes much larger due to the addition of cross-flow momentum. In Hoult et al. [10], plumes originating from a smokestack at the outer edge of the atmospheric boundary layer were examined using an entrainment coefficient of $\alpha = 0.15$ to determine trajectory and mixing with cross-wind. Such variability in the closure argument illustrates the importance of identifying a reliable term to model strong plumes.

When a plume reaches the point of buoyancy and is quasi horizontal traveling parallel to the flow, the entrainment coefficient of a strong plume, α, was too small to properly model the entrainment of air [6]. A second dimensionless coefficient, β, was introduced to describe the dominant horizontal movement of the plume. Similar to the variations of the entrainment coefficient in strong plumes, β is highly dependent on the conditions of the case being examined. Briggs compared photographic data of plume depth versus rise, where the best fit for bent plume trajectories was found to be $\beta = 0.6$. [6] This result applies to the dynamic radius which includes the effective mass outside the plume. For the smokestack experiment in Hoult et al. [10], several values of β were used to determine the best fit based of a set α. It was found that $\beta = 0.60$ was the optimal laboratory experimental value but produced higher error when determining the plume rise compared to $\beta = 0.90$.

When examining the third section of the plume, or bending plume, there exists a

transition from ejection velocity to cross-flow dominating the movement of the plume. Because both entrainment coefficients can describe the plumes motion, the assumption was made that α and β are additive.

The study of bending plumes, or jets in cross flow, has been examined since the mid-20th century [13, 14]. Early work on the understanding of bending plumes can be seen in the works of Keffer and Baines [11] where the development of the plume was examined and explained using a single function. This work was expanded in Chassaing et al. [7] and Andreopoulos and Rodi [1] to measure the velocity field of a jet in cross-flow at different velocity ratios, and New et al. [18], who examined the velocity fields of different jet shapes in cross-flow. In Briggs et al. [6], the trajectory of the plume was found to follow a two thirds power law. This description of the trajectory involved the entrainment of the ambient air obtained from experimental and simulation results (see Zhang and Ghoniem [25]).

Understanding of the entrainment along the entire trajectory of a plume is still imperfect due to the uncertainty of the location of the edge of the shear layer, known as the Corrsin superlayer [8]. Experiments have been done to examine the velocity fields within a plume (see Su and Mungal [22] and Moussa et al. [17]), but by experimentally examining both the plume and cross-flow together, identifying the boundary of the plumes column, the entrainment of the ambient air can be determined for bending plumes in various conditions.

Chapter 2

Turbulence and Volcanic Theory

Equations behind the analysis of the turbulent flows and volcanic plume entrainment are presented here in. By understanding the fundamental characteristics of these topics, the results presented in Chapter 4 are quantified using accepted theory.

2.1 Reynolds-Averaged Navier-Stokes Equation for Turbulent Flow

The examination of a collection of instantaneous vector fields is best understood when it is represented in terms of mean flows and stresses. Reynolds decomposition is employed to define the instantaneous velocity, $\tilde{u}_i$, as the sum of the mean, $\bar{u}_i$ and fluctuations, u_i'. With three dimensional data, the instantaneous field is represented in three components,

$$\tilde{u} = \bar{u} + u' \qquad \tilde{v} = \bar{v} + v' \qquad \tilde{w} = \bar{w} + w', \tag{2.1}$$

where u is the streamwise velocity, v is the vertical velocity and w is the out-of-plane velocity. This provides the mean vector field and a collection of fluctuation field samples.

In this investigation, the mean flow is used to describe the interaction of a jet whose

exit is orthogonally oriented to a cross-flow. By substituting the Reynolds decomposition into the equation and averaging the entire equation, the flow is described using the Reynolds Averaged Navier-Stokes (RANS) equation,

$$\frac{\partial \bar{u}_i}{\partial t} + \bar{u}_j \frac{\partial \bar{u}_i}{\partial x_j} = -\frac{1}{\rho}\frac{\partial \bar{p}}{\partial x_i} + \nu \frac{\partial^2 \bar{u}_i}{\partial x_j^2} + \frac{\partial}{\partial x_j}\left[-\overline{u_i' u_j'}\right]. \tag{2.2}$$

Assuming uniform pressure, time-independent flow and negligible viscous terms, we reduce the equation to the form

$$\bar{u}_j \frac{\partial \bar{u}_i}{\partial x_j} = \frac{\partial}{\partial x_j}\left[-\overline{u_i' u_j'}\right]. \tag{2.3}$$

The term on the right hand side of the equation is the Reynolds stress tensor which is represented by its spatial terms,

$$\overline{u_i' u_j'} = \begin{pmatrix} \overline{u'u'} & \overline{u'v'} & \overline{u'w'} \\ & \overline{v'v'} & \overline{v'w'} \\ & & \overline{w'w'} \end{pmatrix}. \tag{2.4}$$

The diagonal of the Reynolds stress tensor is used to compute the turbulent kinetic energy of the flow, k, defined as,

$$k = \frac{1}{2}\left(\overline{u_i' u_i'}\right) = \frac{1}{2}\left(\overline{u'^2} + \overline{v'^2} + \overline{w'^2}\right). \tag{2.5}$$

This identifies turbulent kinetic energy production within a vector field which is used to isolate key structures and dominant stress terms within a complex flow. Through the expansion of the RANS equation for each component, non-dominant

terms are neglected by examining the magnitudes of each derivative term. The evaluation of the RANS equation from a sample case is seen in Appendix C. Analysis shows the x-momentum equation has four dominant terms,

$$\bar{u}\frac{\partial \bar{u}}{\partial x} + \bar{v}\frac{\partial \bar{u}}{\partial y} = -\frac{\partial}{\partial x}\overline{u'u'} - \frac{\partial}{\partial y}\overline{u'v'}, \tag{2.6}$$

the y-momentum has two dominant terms,

$$\bar{v}\frac{\partial \bar{v}}{\partial y} = -\frac{\partial}{\partial y}\left[\overline{v'v'}\right], \tag{2.7}$$

and the w-momentum has four dominant terms,

$$\bar{u}\frac{\partial \bar{w}}{\partial x} + \bar{v}\frac{\partial \bar{w}}{\partial y} = -\frac{\partial}{\partial x}\overline{u'w'} - \frac{\partial}{\partial y}\overline{v'w'}. \tag{2.8}$$

By combining the stresses and turbulent kinetic energy, the production of turbulence within the plume is understood. The analysis of the mean flow field and Reynolds stresses are performed to provided information on entrainment analysis.

2.2 Entrainment

Understanding the entrainment of ambient air in a bending plume is the focus of this work. Within the plume, there are three distinct regions of interest, each with different components of dominant mixing. For the first region, a strong plume in ambient fluid, the entrainment is measured as the ratio of the entrained velocity perpendicular

to the plume, v_e, and the mean plume exit velocity, v_{jet}, defined as

$$\alpha = \frac{v_e}{v_{\text{jet}}} \tag{2.9}$$

and seen below in Figure 2.1. The entrained velocity is measured at the edge of the Corrsin superlayer of the plume, which is identified as the first location of shear, as seen in Figure 2.2. Moving away from the plume centerline, the shear will decrease after the maximum. The location of negligible velocity fluctuations is the Corrsin superlayer.

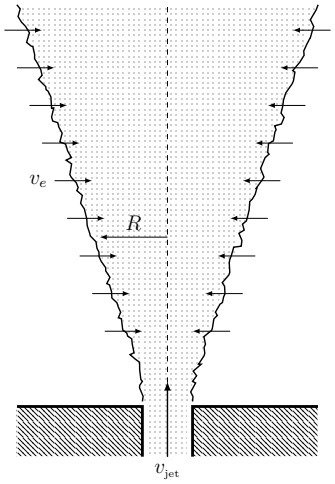

Figure 2.1: Strong plume entrainment

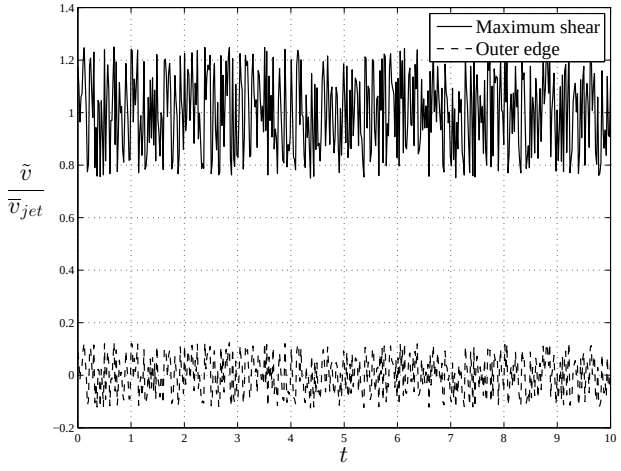

Figure 2.2: Velocity for an axisymmetric jet

When the plume reaches a buoyant state and the cross-flow component dominates the motion of the plume, the entrainment coefficient α does not satisfy the Taylor entrainment approximation. It is instead replaced with the entrainment coefficient for

vertically entrained fluid, β, defined as,

$$\beta = \frac{v_e}{v_c}. \tag{2.10}$$

where v_c is the vertical velocity of the plume centerline (Figure 2.3). At this stage, the Corrsin superlayer of the plume is indistinguishable due to the core of the plume collapsing into a turbulent shear layer.

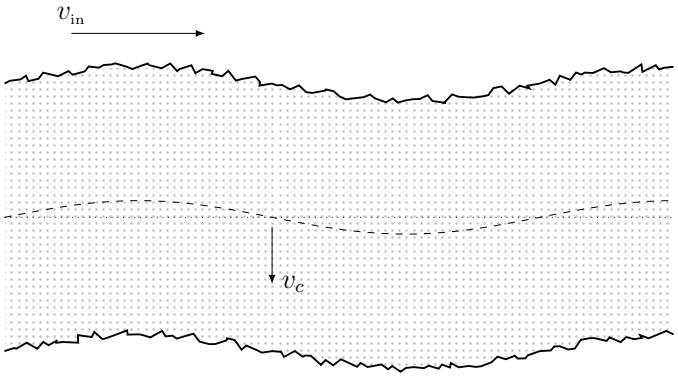

Figure 2.3: Bent plume entrainment

Both α and β have been experimentally examined and play a role in the trajectory of a bending plume under the influence of a cross-flow.

The third region, a bending plume, is found between the strong plume and bent plume region (Figure 2.4). For this region, the terms α and β were both incorporated in models of entrainment by means of the mass balance

$$\frac{\mathrm{d}M}{\mathrm{d}s} = 2\pi r \rho_{\text{amb}} \left(\alpha v_{\text{jet}} - v_{\parallel} + \beta v_{\perp} \right) \tag{2.11}$$

where $v_{\parallel}$ and $v_{\perp}$ are the velocity components parallel and perpendicular to plume centerline respectively.

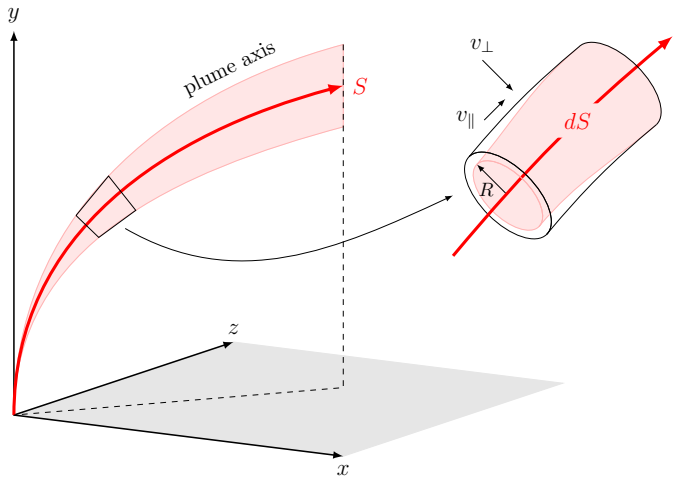

Figure 2.4: Bending plume control volume

In Briggs, [6] the centerline of a buoyant plume in cross-flow was described using non-dimensional spatial coordinates x/l_b and y/l_b, as the downstream axial location and the centerline rise of the plume, respectively. The scaling length used is known as the buoyancy length, defined as

$$l_b = \left|\frac{\rho_p}{\rho_0}\right| \frac{gD^2}{4v_{\text{in}}^2}, \tag{2.12}$$

where ρ_p and ρ_0 are the plume and ambient air density, respectively, g is the acceleration due to gravity and D is the diameter of the plume. Briggs found that the centerline rise follows the two-thirds law,

$$\frac{y}{l_b} = \left(\frac{3}{2\beta^2}\right)^{1/3} \left(\frac{x}{l_b}\right)^{2/3}. \tag{2.13}$$

This provides an initial guess when fitting plume centerline data.

Plume entrainment theory directs the analysis performed in Chapter 4 on the tra-

jectory and components of velocity relative to the centerline of a jet in cross-flow.

Chapter 3

Experimental Setup

3.1 Wind tunnel facility

The facility at Portland State University was designed to help research fundamental and applied cases of turbulent fluid flows. The facility consists of a closed-circuit wind tunnel with a contraction ratio of 9:1 to prevent noticeable turbulence intensities in an open test section. The test section has a length of 5 m and a cross section of 0.8 m × 1.2 m. The free-stream wind speed has a adjustable working range of 2 m/s to 20 m/s in the test section. The test section is comprised of a variable-profile articulated ceiling, fixed non-operators'-side wall, replaceable floor panels, and operators-side wall consisting of access panels. At the entrance to the test section, an active grid system comprised of 10 cm square winglets attached to 6 horizontal and 7 vertical rods is used to add turbulence to the free-stream flow. Each rod is connected to a closed-loop motor with independent rotational capabilities input through LabView protocol. For these experiments, passive grid is used to describe no winglet movement while active grid indicates motors input and rotation. For the active grid cases, the motors were given a new rotation speed every second with an upper limit of ±2 RPS and a lower limit of ±0.5 RPS. Passive grid indicates a turbulence intensity of 5% while active grid indicates

a turbulence intensity of 20 – 30%

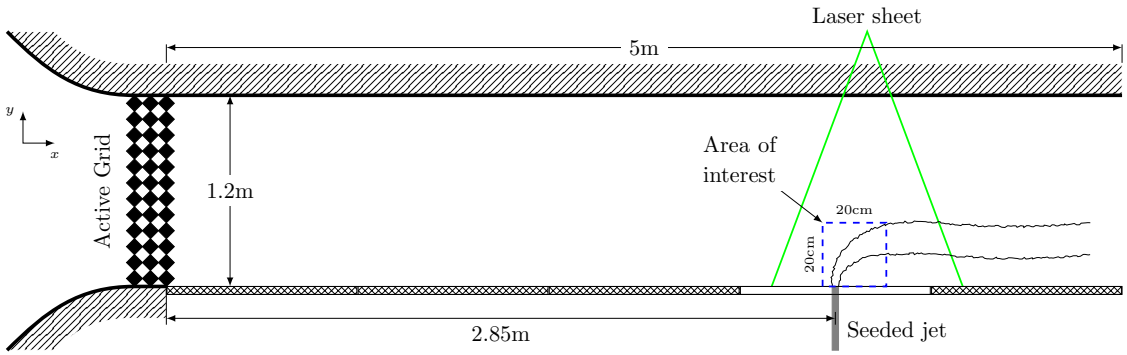

Figure 3.1: Schematic of PSU Wind Tunnel Test Section

A floor panel was replaced with an acrylic sheet machined to allow for a jet of air to enter the test section perpendicular to the free-stream flow at $y = 0$. Compressed air is fed through a pressure regulator with an adjustable valve to control jet velocity and is injected into the test section. A seeding line is added to the jet prior to the exit to allow for thorough mixing of the air and seed (Figure 3.2).

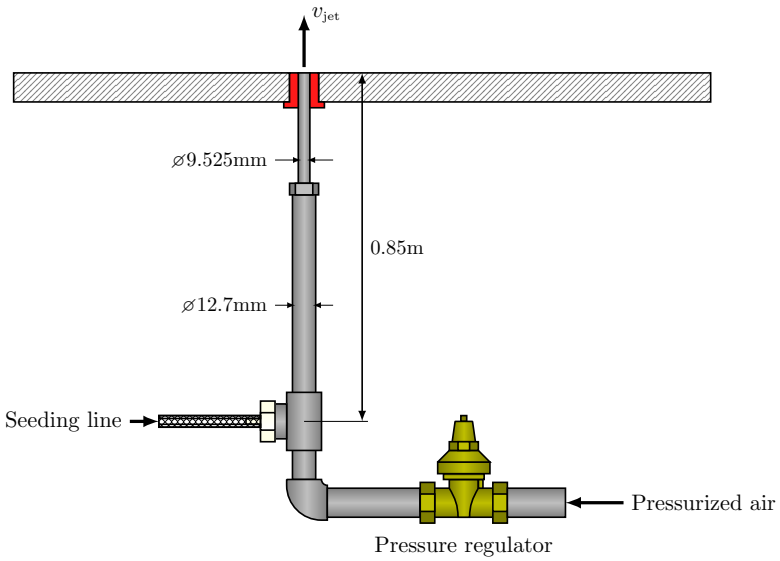

Figure 3.2: Experimental setup of jet system

3.2 Instrumentation

The SPIV data in this experiment was collected within one window focused on the exit of the jet of air as seen in Figure 3.1. The SPIV setup consisted of LaVision system with an Nd:Yag (532 nm, 1200 mJ, 4 ns duration) double-pulsed laser and two 4MP ImagerProX CCD cameras arranged to allow stereoscopic measurements of the jet. The jet was seeded with neutrally buoyant fluid particles (diethylhexyl sebacate) and allowed to mix with the free-stream flow.

Cameras were calibrated before each measurement set using a standard two-plane measurement plate with specific geometries (Type 22) recognized by DaVis PIV software. The resulting measurement window was approximately 0.2 m × 0.2 m with a vector resolution of approximately 1.5 mm.

To ensure convergence to a mean, 1500 SPIV image sets were collected for passive grid cases, and 2500 for active grid turbulent cases. Raw images were processed into vector fields using a multi-pass FFT based correlation algorithm of reducing size interrogation windows (twice at 64 × 64 and twice at 32 × 32 pixels) with a 50% overlap. The first two passes were evaluated using a square interrogation window and the final two using a 4:1 vertical gaussian envelope to capture high speeds at the exit of the jet. For each experiment, two delays between image pairs were set, one to focus on the interaction of the plume and free-stream flow, and a second varying delay to measure the free-stream flow.

3.3 Experiment Settings

To understand the influence of free-stream velocity and turbulence on the development of plume, experimental data was taken at several different inflow speeds using both a passive and an active grid protocol. The speed of the jet was kept constant to develop a ratio of jet speed, v_{jet}, to cross-flow speed, v_{in}, defined as

$$R_v = v_{\text{jet}} / v_{\text{in}}. \tag{3.1}$$

For both passive and active grid, seven different settings were used for the wind tunnel to produce a range of different ratios (Table 3.1).

Passive Grid			**Active Grid**		
v_{in} (m/s)	v_{jet} (m/s)	R_v	v_{in} (m/s)	v_{jet} (m/s)	R_v
1.153	39.52	34.3	1.563	40.85	26.1
2.060	41.21	20.0	1.974	41.54	21.0
2.967	40.28	13.6	2.386	40.67	17.1
3.874	40.74	10.5	2.797	41.22	14.7
4.780	39.56	8.28	3.208	40.69	12.7
5.687	40.68	7.15	4.030	41.47	10.3
6.594	41.07	6.23	4.853	41.26	8.50

Table 3.1: Inflow and jet velocities and corresponding ratios for Passive and Active Grid experiments

Each test produced a mean vector field for velocities, Reynolds stresses and shear stresses. One case of high R_v and one case of low R_v will be presented for both active and passive grid. This will highlight the differences high turbulence intensity has on the development of the plume.

Chapter 4

Results

Results of the SPIV data for mean statistics of velocity and Reynolds stresses are presented here. Further analysis of plume trajectories and profile analysis is compiled to quantitatively describe the effects of various jet to cross-flow ratios and its influence on mixing of ambient fluids with the plume (entrainment).

4.1 Mean flow statistics

The processed data from PIV analysis is presented in Figures 4.1-4.4. The results were normalized to allow for direct comparison. The spatial axes were non-dimensionalized by the diameter of the jet, D, while the velocity components were non-dimensionalized by the speed of the jet at the exit, v_{jet}. The window was trimmed to focus on the bending plume section and presented on a square grid to represent the length scales accurately. The results are presented for a range of inflow conditions represented as

$$R_v = \frac{v_{\text{jet}}}{v_{\text{in}}}.$$

For two similar ratios of passive ($R_v = 20,\ 10.5$) and active grid ($R_v = 21,\ 10.3$), comparisons are made to describe key interactions within the flow-field.

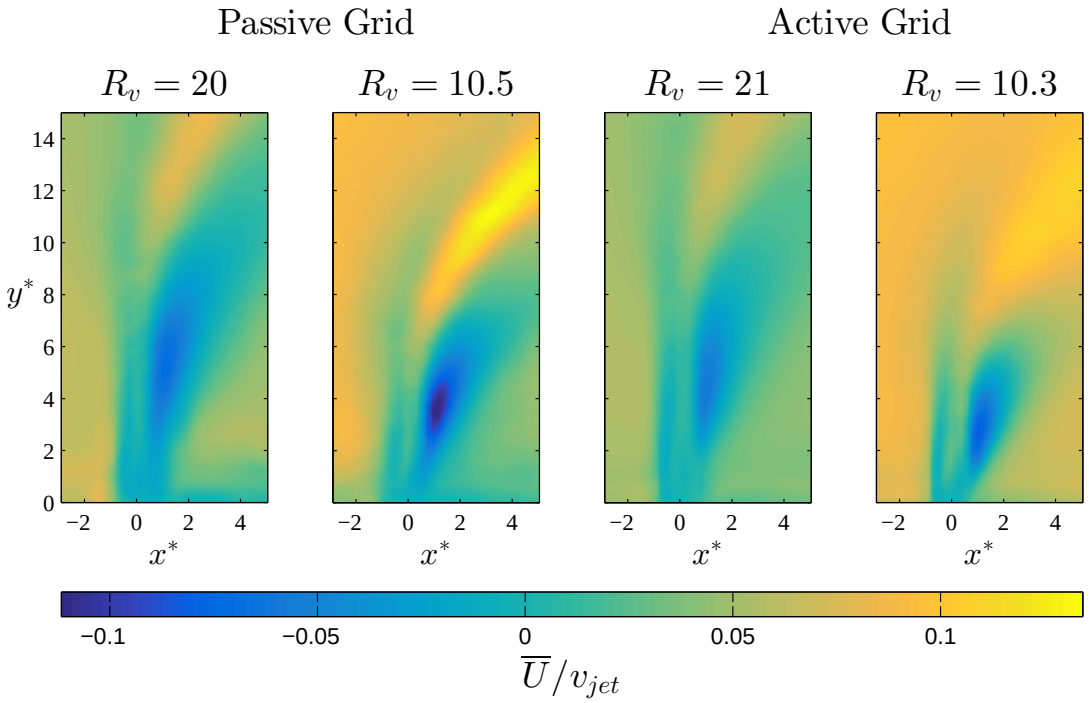

Figure 4.1: Passive grid (left two ratios) and active grid (right two ratios) contour plots of mean downstream velocity

For the downstream velocity component shown in Figure 4.1, there are four regions of interest (see Figure 4.2).

At the exit of the jet ($y^* = 0$), there is no axial velocity within the boundary of the jet. This is consistent with the characteristics of a strong plume, where the exit velocity is unaffected by the cross-flow velocity. Upstream of the jet, in region 1, the cross-flow is moving at a constant velocity entering the window and approaching the jet. At $x^* \approx -0.5D$, the velocity drops to zero, indicating the cross-flow reaches a stagnation point at the upstream edge of the jet. This stagnation point indicates that the cross-flow treats the jet as a bluff body and cannot move through it. Downstream of the jet in region 2, the flow returns to the cross-flow velocity, indicating the flow is moving

around the jet and reentering the plane downstream.

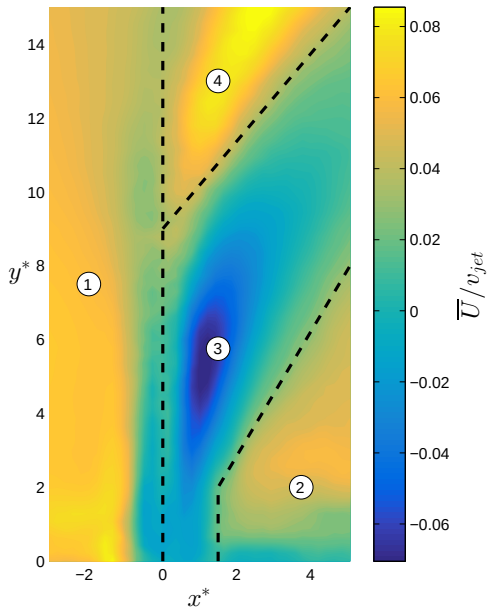

Figure 4.2: $\bar{U}$ regions of interest

In region 3, downstream of the jet ($x^* > 0.5$), a region of negative velocity shows the flow is moving back into the jet. Combining the negative velocity with the stagnation point observation, the cross-flow is found to recirculate in an eddy of fluid downstream of the jet. A maximum negative velocity is identified that is equal in magnitude to the cross-flow above the exit of the jet. As R_v is decreased for both passive and active grid, the maximum occurs closer to the exit of the jet and begins to dissipate and move downstream earlier (as y^* increases). This indicates that the wake is connected to the rate the jet is bending downstream.

As the jet develops in the $+y^*$ dimension (region 4), the $\bar{U}$ component reaches a maximum as the jet bends downstream with the negative flow region just below it. As R_v is decreased, both of these regions bend downstream earlier, indicating that the

downstream shear layer of the jet is traced by the boundary of these two regions. Between the two passive cases, the boundary of the two regions shift down at the edge of the window from $y* \sim 14D$ to $y^* \sim 11D$. As this boundary shifts down, the maximum $\bar{U}$ velocity within the jet itself increases (2 fold for passive cases).

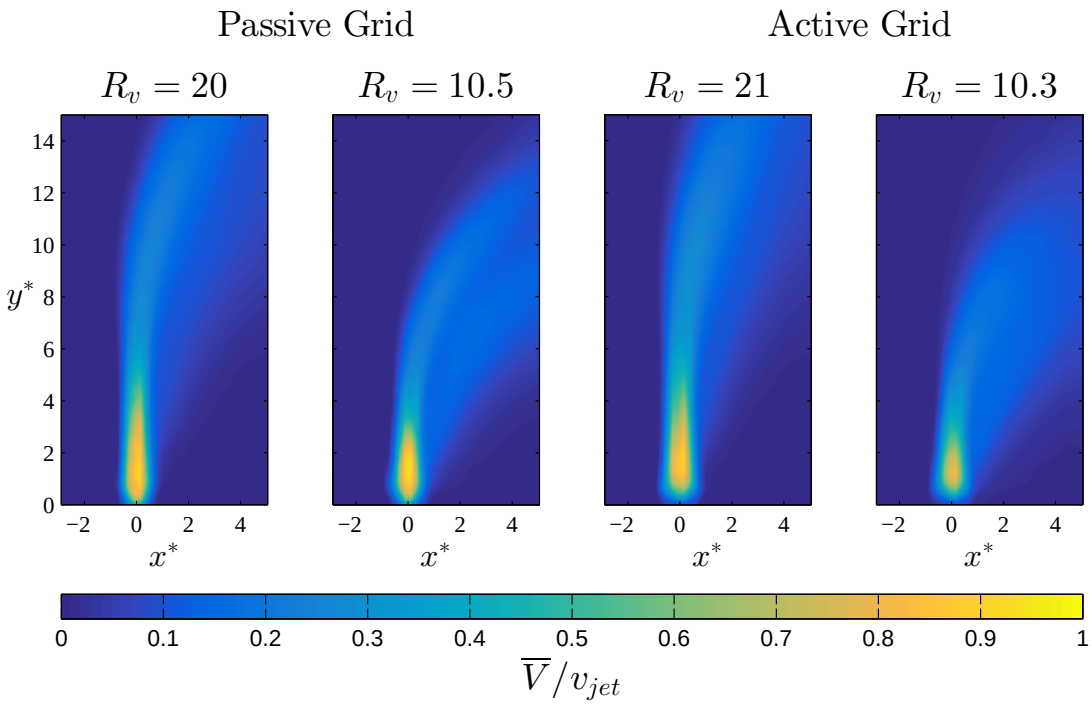

Figure 4.3: Passive grid (left two ratios) and active grid (right two ratios) contour plots of mean vertical velocity

In the second mean flow component, $\bar{V}$, the comparison of weak to strong plume is made. Prior research of strong plume's in zero cross-flow has shown that as air is ejected vertically, the effects of gravity will slow the $\bar{V}$ component as it moves in the $+y^*$ direction. In Figure 4.3, the results of the vertical velocity analysis for this experiment produced similar results: a decreasing $\bar{V}$ component with an increasing $+y^*$. By non-dimensionalizing the velocity field by the speed of the jet, v_{jet}, the field has a set

domain of $\bar{V}/v_{\text{jet}} = [0,1]$.

The differences between strong and weak plumes are found by comparing the upstream and downstream $\bar{V}$ field. For a jet without cross-flow, the vertical velocity outside the shear layer of the jet will remain zero. In a weak plume, the vertical velocity upstream of the jet will be zero, but downstream, there is a region of growing vertical velocity. As the jet is imparted with the cross-flow velocity, the shedding of fluid with vertical momentum occurs at the boundary of the jet, imparting it with axial velocity in addition to the vertical velocity. The decay of vertical velocity, combined with the axial velocity field, describes the shift of vertical momentum at the exit of the jet to axial momentum as the cross-flow mixes with the jet. As the cross-flow continues to mix with the jet and the vertical momentum is transferred into axial momentum, a neutrally buoyant level will be reached that is known as the bent plume regime.

The final velocity field presented is the $\bar{W}$ component (Figure 4.4), which denotes movement in and out of plane. In the $\bar{W}$ velocity field, two observations are made to enhance the description of cross flow activity. Upstream of the plume, there is a component of $\bar{W}$ just outside the domain of the jet exit which describes the movement of fluid around the plume. Within the plume itself, there is a small component of velocity that is described as the turbulent mixing of fluid.

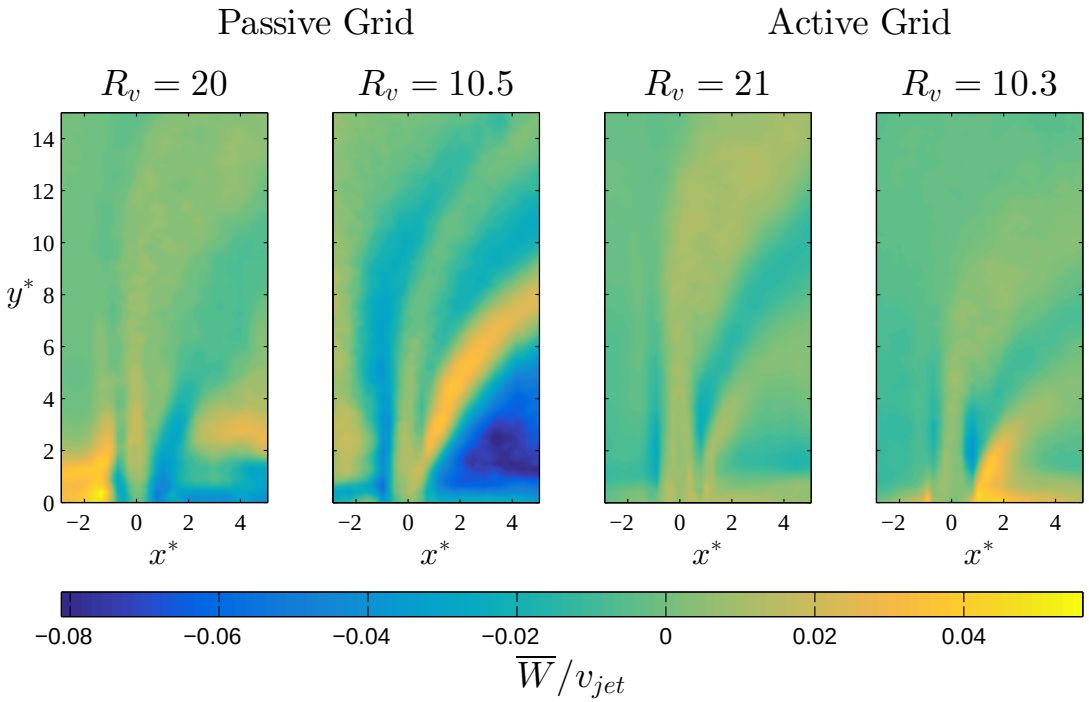

Figure 4.4: Passive grid (left two ratios) and active grid (right two ratios) contour plots of mean out-of-plane velocity

Expanding on the upstream flow movement (Figure 4.1), there is another region of non-zero out-of-plane velocity that indicates the cross-flow reentering the plane. The axial flow moving downstream moves around the plume, reentering the field downstream of the plume and moving upstream into the plume. This means the negative axial flow and out of plane movement downstream of the plume is a wake created by the plume acting as a bluff body.

4.2 Reynolds stresses and turbulent kinetic energy

In order to describe the influence of turbulence on the flow-field, the Reynolds stresses are presented below. Each stress is normalized by the square of the jet exit

velocity, v_{jet}^2.

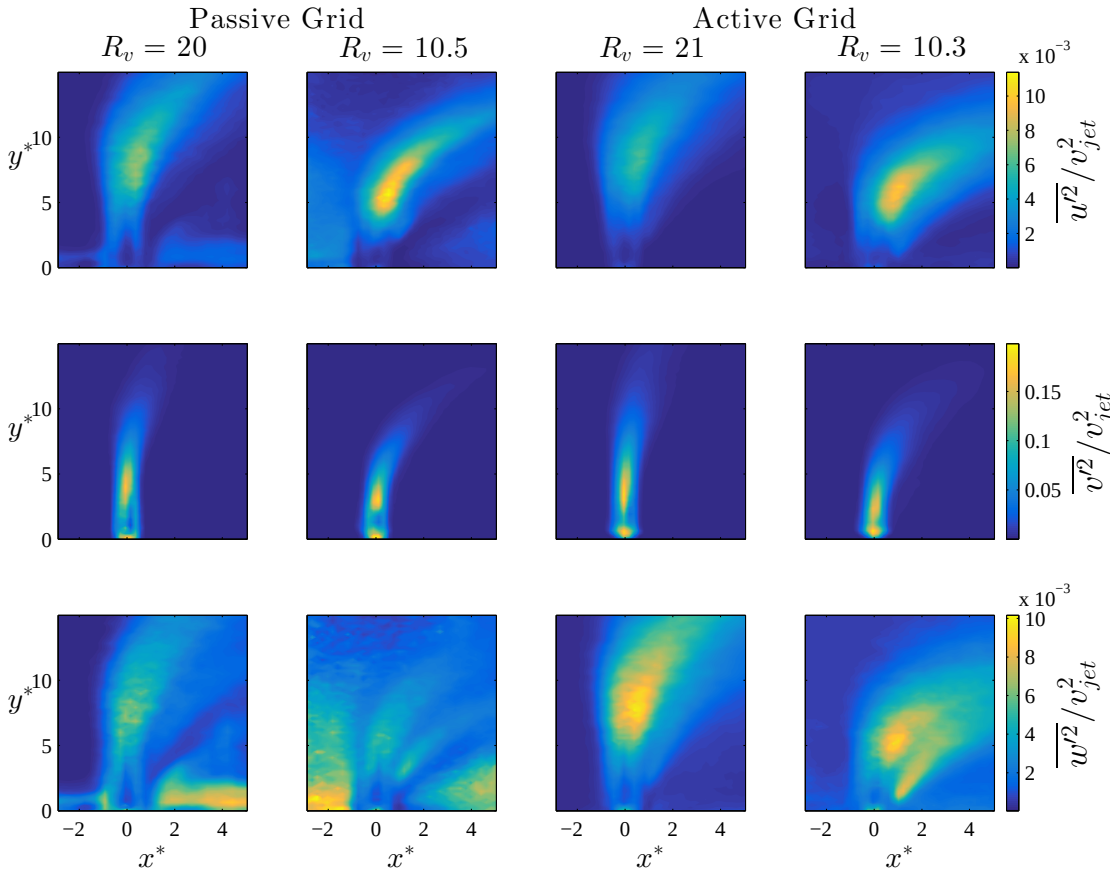

Figure 4.5: Passive grid (left two ratios) and active grid (right two ratios) contour plots of $\overline{u'u'}$, $\overline{v'v'}$, $\overline{w'w'}$

Examining the Reynolds normal stresses of the jet and cross-flow for the passive grid cases (Figure 4.5), the first indicator of turbulent production is found in the $\overline{v'v'}$ component, which highlights the vertical growth of the jet. At the exit of the jet, there is a region of negligible stress that is best identified as the potential core of the jet, a region unaffected by the cross-flow. After the collapse of the potential core, the maximum stress is reached, indicating a large fluctuation in the vertical component of the velocity field. As the jet develops, the stresses decrease similarly to the velocity field, $\bar{V}$,

but maintain the slender shape of the body of the plume. This decay of vertical normal stress is and indicator of the edge of the upstream shear layer as the jet develops.

The axial normal stress, $\overline{u'u'}$ identifies the transition point to bending plume found in the previous section. In the jet, the axial stress is very low until the cross-flow begins to bend the jet downstream. Combining it with the $\overline{v'v'}$ field, the axial stress reaches a maximum just after the maximum of the vertical stress. Comparing different ratios, this location of maximum stress moves closer to the exit of the jet, indicating an earlier transition point to the bending plume regime. As R_v is decreased, the magnitude of these terms also increase (approximately 2 fold) to show the generation of axial turbulence increases as the cross-flow speed increases.

For the final term, $\overline{w'w'}$, the out-of-plane normal stress, the structure of the jet is present, as well as some regions outside the plume. This normal stress component illustrates the spread of the jet as it develops, and reaches a maximum within the jet at the same location as the $\overline{u'u'}$ term. This shift between dominant stresses highlights the normal stresses are important in identifying the turbulence production as the jet transitions from the strong plume to bending plume regime.

Reynolds shear stresses are presented below in Figure 4.6.

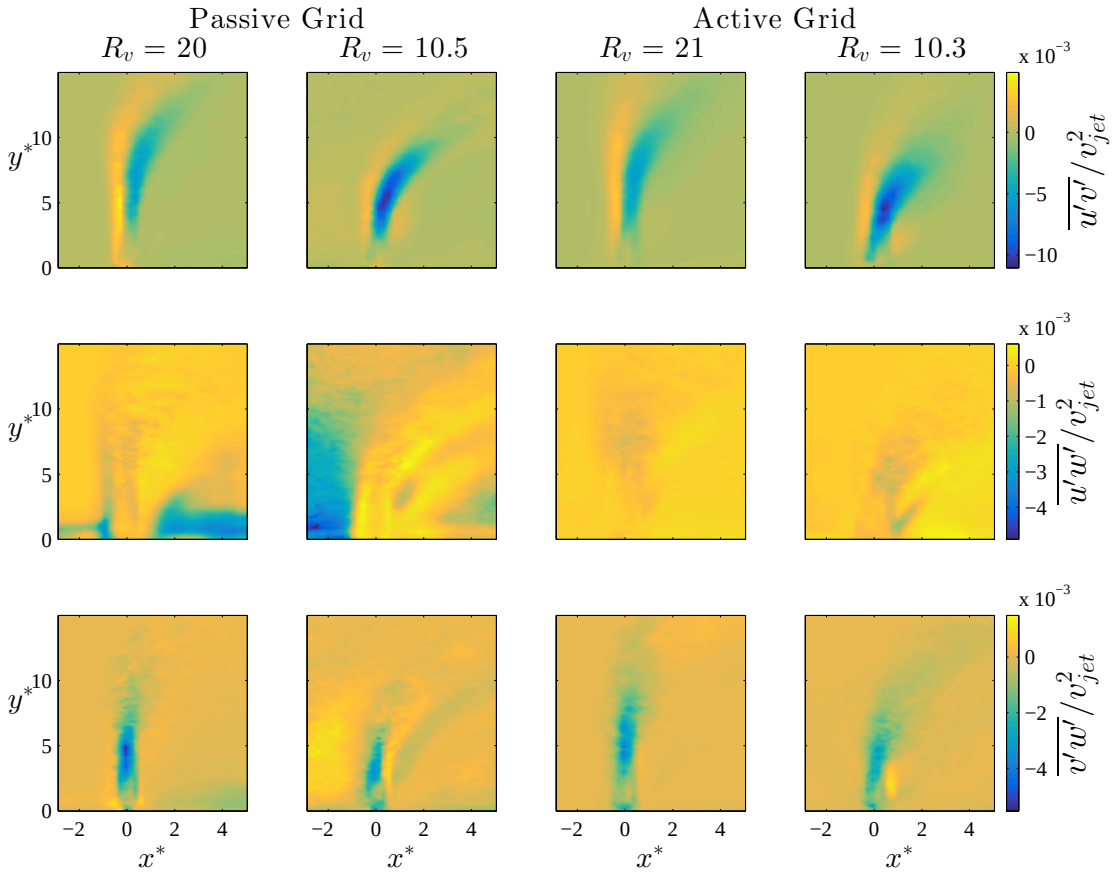

Figure 4.6: Passive grid (left two ratios) and active grid (right two ratios) contour plots of $\overline{u'v'}$, $\overline{u'w'}$, $\overline{v'w'}$

The shear stress, $\overline{u'v'}$, is the most dominant shear stress with a magnitude twice as large as the out-of-plane shear stresses. The $\overline{u'v'}$ term has two distinct regions, one upstream of the jet centerline that is positive and one downstream that is negative. As the jet develops, this term reaches a maximum that corresponds to the same transition point observed in the normal stresses, indicating this is the location of the collapse of the potential core of the jet. The positive and negative regions have a clear boundary between them and is determined to be the centerline of the plume, with a spreading shear region on either side.

The shear stress component $\overline{u'w'}$ measures the activity outside the plume, the movement of fluid around the bluff body and reentering of fluid behind in a wake. There is negligible shear stress within the plume, confirming the axial and out-of-plane movement of fluid is produced by the cross-flow. Finally, when examining the $\overline{v'w'}$ component, the upstream minimum indicates an interaction of the shear layer with the cross-flow movement around the plume. Downstream, a region of insignificant stress occurs within the wake and the edge of the plume as it is bending downstream.

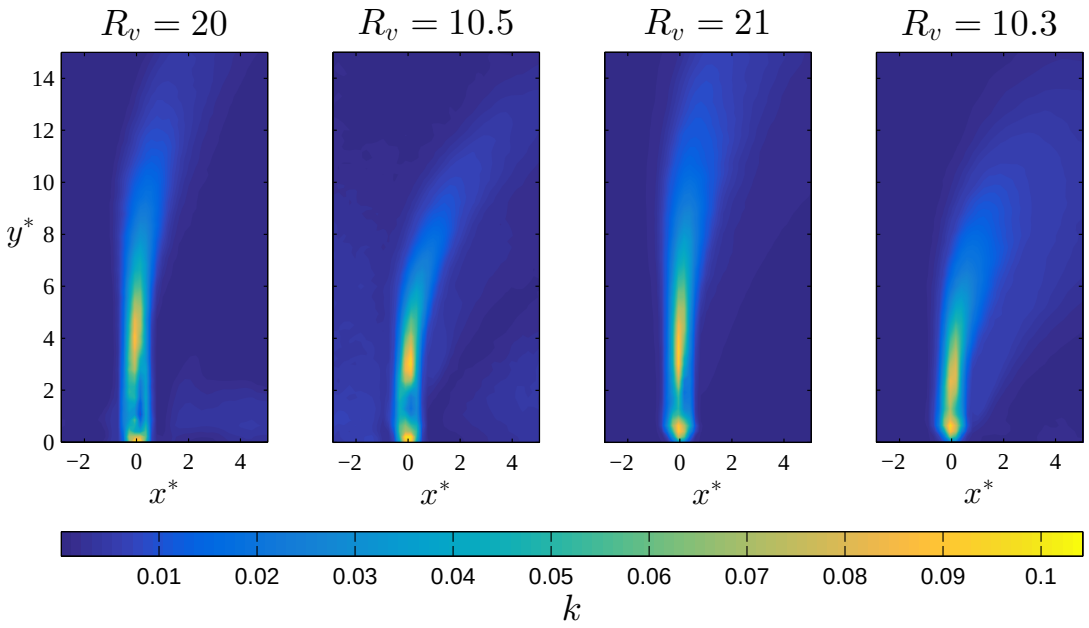

Figure 4.7: Passive grid (left two ratios) and active grid (right two ratios) contour plots of the turbulent kinetic energy, k

Figure 4.7 shows the combination of Reynolds normal stresses to create the turbulent kinetic energy field, k, where the structure of the jet is dominant . This indicates the jet creates turbulence within the body of the plume as it moves upstream as well as a growing region downstream. The elongation of the high turbulence region in the

plume illustrates the effect of the growth of the turbulent shear layer within the plume.

Comparing the passive to the active grid Reynolds stresses, the properties are similar. The body of the plume is dominant in the generation of turbulent kinetic energy and its structure is easily identifiable. What stands out is the magnitude of the stresses within the active grid plume is approximately 25% smaller when comparing the axial components, indicating the increase in cross-flow turbulence intensity reduces the development of turbulence within the jet as it develops.

By understanding the influence of the generation of turbulence within the jet, the development of a jet in cross flow is characterized. The next step is to quantify the differences identified between ratios and the passive and active grid.

4.3 Modeling plume development

When analyzing the characteristics of the plume, the first step is determining the difference in the bending of the plume. The center of the jet exit is found by using the vector field data and using the streamline interpolation method outlined in Appendix D. Creating a streamline from the center of the jet exit, $(x^*, y^*) = (0,0)$, to the edge of the window allows the trajectory of a plume in a cross-flow of various inflow conditions to be described. These values are then used to establish a centerline of the plume to be used in further analysis.

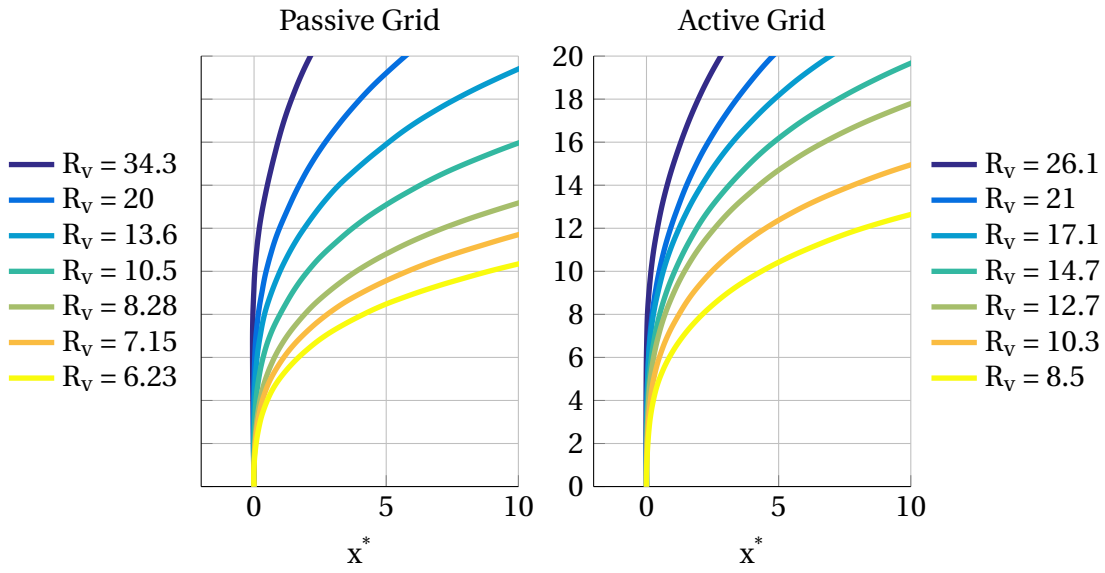

Figure 4.8: Streamline trajectory of the plume centerline for varying R_v

In Figure 4.8, the trajectory of the plume changes with R_v. As R_v is decreased ($R_v \rightarrow 1$), the plume bends at a faster rate while the region of purely vertical movement decreases. This will be a key factor in identifying the differences cross-flow velocity has on the trajectory of the plume.

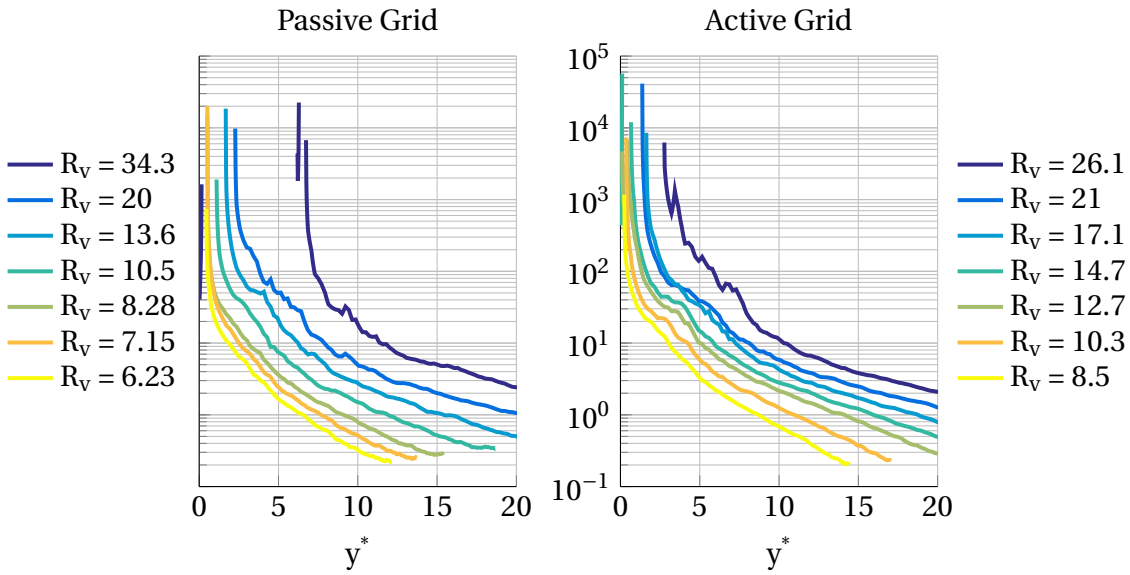

Figure 4.9: Slope of the plume centerline

In order to describe each trajectory, the slope of the line is calculated to note any fundamental indicators of an ideal equation to fit the streamline. Each case showed a decreasing positive slope from an asymptote ($dy^*/dx^* = \infty$) at decreasing y^* as R_v decrease. The asymptote is interpreted as the transition point where the jet begins to bend downstream. The jet must then be described as a two-part piece-wise function: the exit to the transition point of a bending plume (where $dy^*/dx^* \to \infty$), and the transition point to the end of the interrogation area.

From the observations made using the slope of the streamline, and a least-mean squares approach to solve for a coefficient and exponent is employed by using an equation of the form

$$y^* = y_t^* + A\left(x^*\right)^B \tag{4.1}$$

where y_t^* is the height at which the plume begins its transition to bending plume (Figure 4.10). This equation was chosen from Briggs's two-thirds power law theory which

provides a first approximation of $B = 2/3$. The data collected on the transition point shows a clear relationship between the speed ratio, R_v, and the transition point. The big difference that can immediately be found is the difference between the passive and active grid cases, where the active grid appears to bend much earlier than the passive grid cases. This indicates that the turbulence intensity (and length scales) may be able to converge the data and with more data collection, it would be possible to determine the transition point using the speed ratio and turbulence intensity.

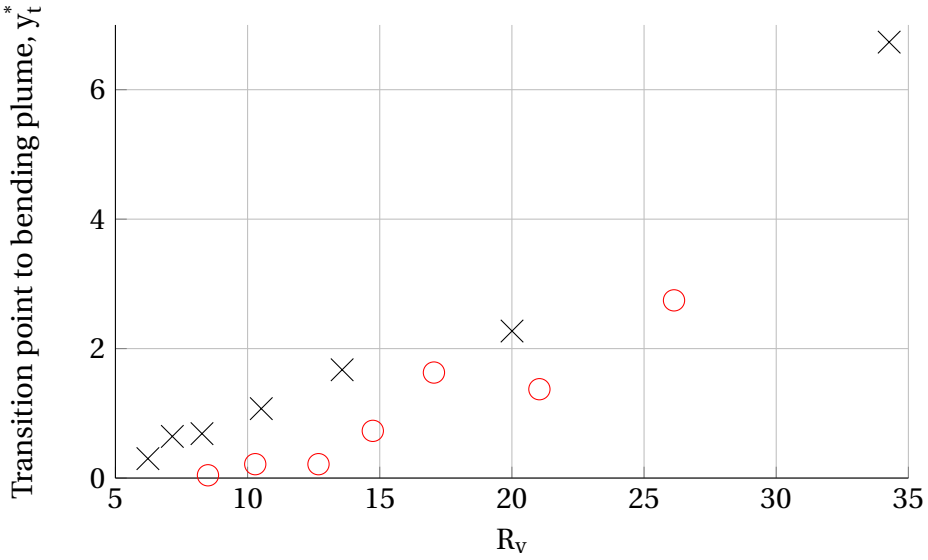

Figure 4.10: Transition point to bending plume for passive grid (×) and active grid (○)

The first coefficient from the fit, A, is presented in Figure 4.11(A). The coefficient, similar to the transition point, has a clear trend with small differences between the passive and active grid. What stands out is the almost linear relationship between the speed ratio and the coefficient, A. This reduces the complexity of the relationship between A, the ratio, R_v, and the turbulence intensity.

In Figure 4.11(B) the exponent B, is presented, which was given an initial approxi-

mation of 1/1.5 using Brigg's two-thirds theory. While the relationship between R_v and B is not clear, the exponent is almost twice as large as initially predicted from theory. The exponent exists within the range $B = [1/3.15, 1/3.6]$ but a clear relationship cannot be identified with the current data.

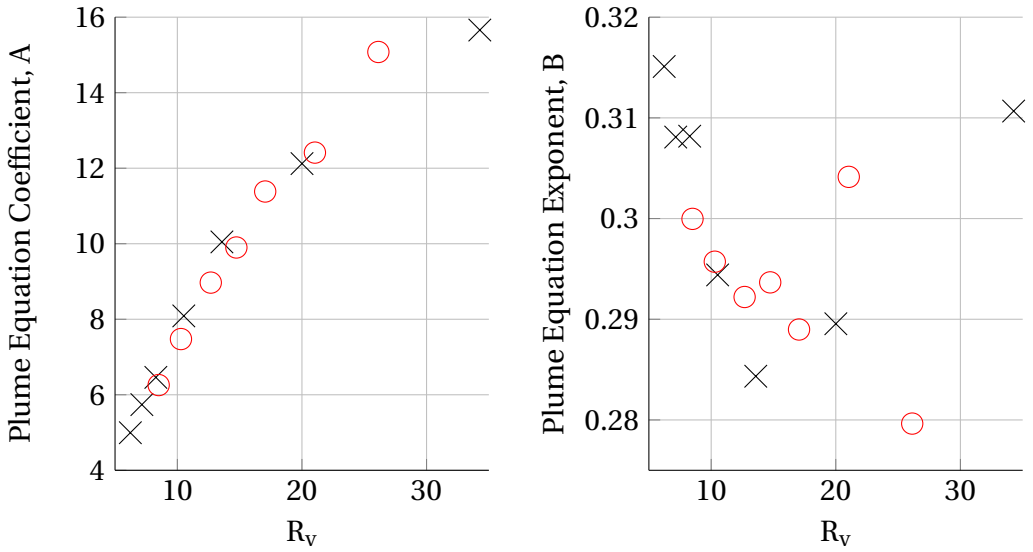

(A) Plume coefficient, A

(B) Plume exponent, B

Figure 4.11: Plume equation coefficients and exponents for passive grid (×) and active grid (○)

By quantifying the trajectory of the jet in cross-flow, further analysis is done to quantify the phenomenon identified in Section 4.1

4.4 Centerline component analysis

To accurately compare the statistics of two jets with different ratios, streamline interpolation is used to trace along the plume centerline. Evaluating the flow field across $[-3D, 3D]$ perpendicular to the centerline at increments of jet centerline length, L^*,

the jet is straightened to allow for comparison between different inflow conditions. An in-depth description of the method used is presented in Appendix D. The magnitude of the velocity for a similar ratio of passive and active grid is non-dimensionalized by the jet velocity and represented in surface plots.

For the mean velocity fields, previous analyses showed that as the jet develops, it bends downstream. As the plume bends, the components of the $\bar{U}$ velocity change from perpendicular to parallel to the jet. This means an adjustment must be made to use $\bar{U}$ and $\bar{V}$ to compute a velocity component parallel and perpendicular to the plume centerline (see equations in Appendix D for a more thorough description of this computation). Figures 4.12 and 4.13 show the resulting parallel and perpendicular velocity fields respectively.

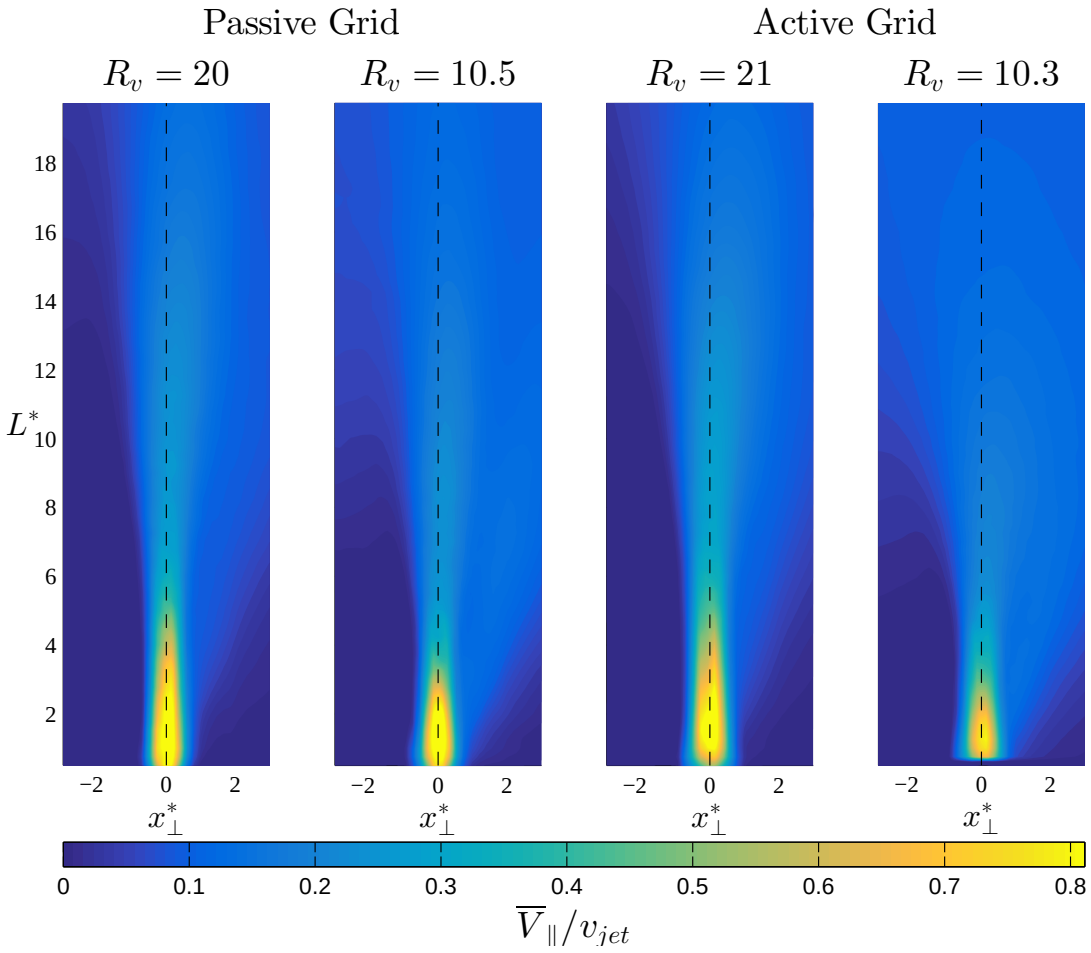

Figure 4.12: Passive grid (left two ratios) and active grid (right two ratios) contour plots of flow moving parallel to the plume centerline

For the flow moving parallel to the jet centerline, there are three regions of interest. The first is at $x_\perp = 0$, the centerline of the plume. The effect of jet decay observed in Figure 4.3 is present in all four panels of Figure 4.12. As the plume develops, the magnitude of the plume's exit velocity decreases similar to that of a strong plume without cross-flow, from $\overline{V}_\parallel \approx 1$ to $\overline{V}_\parallel \approx 0.25$. This demonstrates that as the jet develops, the exit momentum decreases by up to 75% within $20D$ of downstream development.

The second region of interest is the spread of the jet upstream (in the domain $[-3D, 0D]$), which shows the spread of the shear layer of the jet. As the jet moves from the exit along its trajectory, the shear layer should grow upstream. Instead, the edge of the jet only begins to grow after it initially moves inward until it reaches a location where the edge of the jet becomes uniform with the flow outside it. When comparing the different ratios, this location of expansion of the edge of the jet moves closer to the exit of the jet (from $L^* \approx 14$ for $R_v = 20$ and $L^* \approx 7$ for $R_v = 10.5$). This is explained as a location along the trajectory where the $\bar{U}$ velocity component begins to switch orientation from perpendicular to parallel to the plume. This is used as an indicator of the transition to a bending plume.

The third region is upstream of the plume (in the domain $[0, 3D]$) illustrating the effect of a wake (previously defined and discussed in Section 4.1). In this region, the $\bar{V}$ flow-field was observed to spread downstream almost immediately due to the recirculation of the cross-flow. This effect is found again, with parallel flow components spreading much earlier than upstream of the plume. In Figure 4.13, this analysis is expanded by examining the flow perpendicular to the centerline.

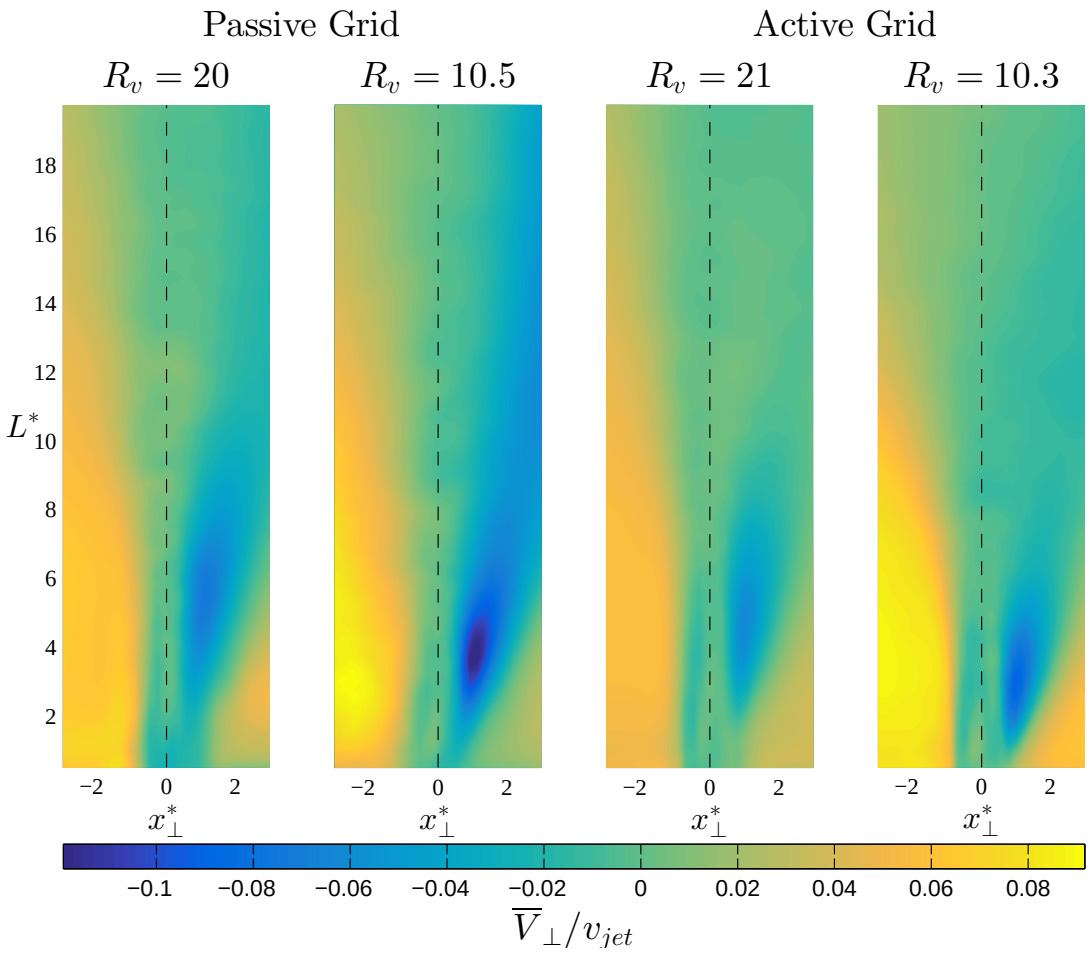

Figure 4.13: Passive grid (left two ratios) and active grid (right two ratios) contour plots of flow moving orthogonally to the plume centerline

The perpendicular velocity field, similar to the parallel velocity field, has three distinct regions of interest. The first is the observation around the centerline, where the flow is negligible, indicating that within the boundary of the plume diameter ($x_\perp = [-0.5D, 0.5D]$]), there is no flow moving into the plume. Along the length of the jet, the centerline velocity remains negligible, which implies that the structure of the jet, compared to a strong plume, has not changed.

Looking upstream of the jet ($x_\perp = [-3D, 0D]$), the cross-flow is present moving towards the centerline of the plume. Moving along the jet's length, the flow moving into the jet decreases. When combined with the $\bar{V}_\parallel$ flow-field, the transition of $\bar{U}$ from perpendicular to parallel is reinforced as the cross-flow component shrinks to approximately 25% the initial $V_\perp$ at $x^*_\perp = -3D$.

Finally, downstream of the jet, similar to the negative $\bar{U}$ region found in Figure 4.1, there is an area of negative velocity fluid moving back into the jet. This negative velocity, or recirculation, expands further from the jet centerline as the jet develops in L^*. As R_v decreases, the maximum within this region occurs closer to the exit of the jet and spreads until, at the edge of the window ($L^* = 20$), all of the flow is negative and moving into the jet.

Comparing upstream and downstream peak magnitudes, the flow is moving approximately equal in magnitude but opposite in direction. For $R_v = 10.5$ (passive grid), the flow moving downstream is approximately $\bar{V}_\perp = 0.1$ and $\bar{V}_\perp = -0.12$ upstream. Compared to a strong jet without cross-flow, the equal and opposite movement of flow into the jet up and downstream is identical.

Both of these components are important when identifying the effects of entrainment of ambient air in the jet. Because entrainment is understood as the ratio of plume speed to ambient air moving perpendicular to the plume, identifying ambient air entering the plume both upstream and downstream of the jet centerline will enhance the understanding of entrainment in bending plumes.

4.5 Stress Development

Plots of the Reynolds stress show how the cross-flow interacts with turbulence in the core of the jet. Figure 4.14 shows the axial normal stress, $\overline{u'u'}$. Within the domain of jet ($x^* = [-0.5, 0.5]$) at the exit of the jet, there is an absence of axial stress. Before the jet transitions to the bending regime, the dominant component is the vertical component of the jet's velocity. When the jet begins to bend, the axial stresses inside the jet reach a maximum indicating the collapse of the potential core. As R_v decreases, the collapse of the potential core occurs closer to the exit of the jet, from $L^* \approx 6D$ to $L^* \approx 4D$. As R_v decreases, the magnitude of the normal stress within the plume is also changing, with almost a 50% increase as R_v is cut in half. This shift of the potential core collapse closer to the exit of the jet and the increase in magnitude highlighting the generation of axial turbulence, is related to the transition point to bending plume.

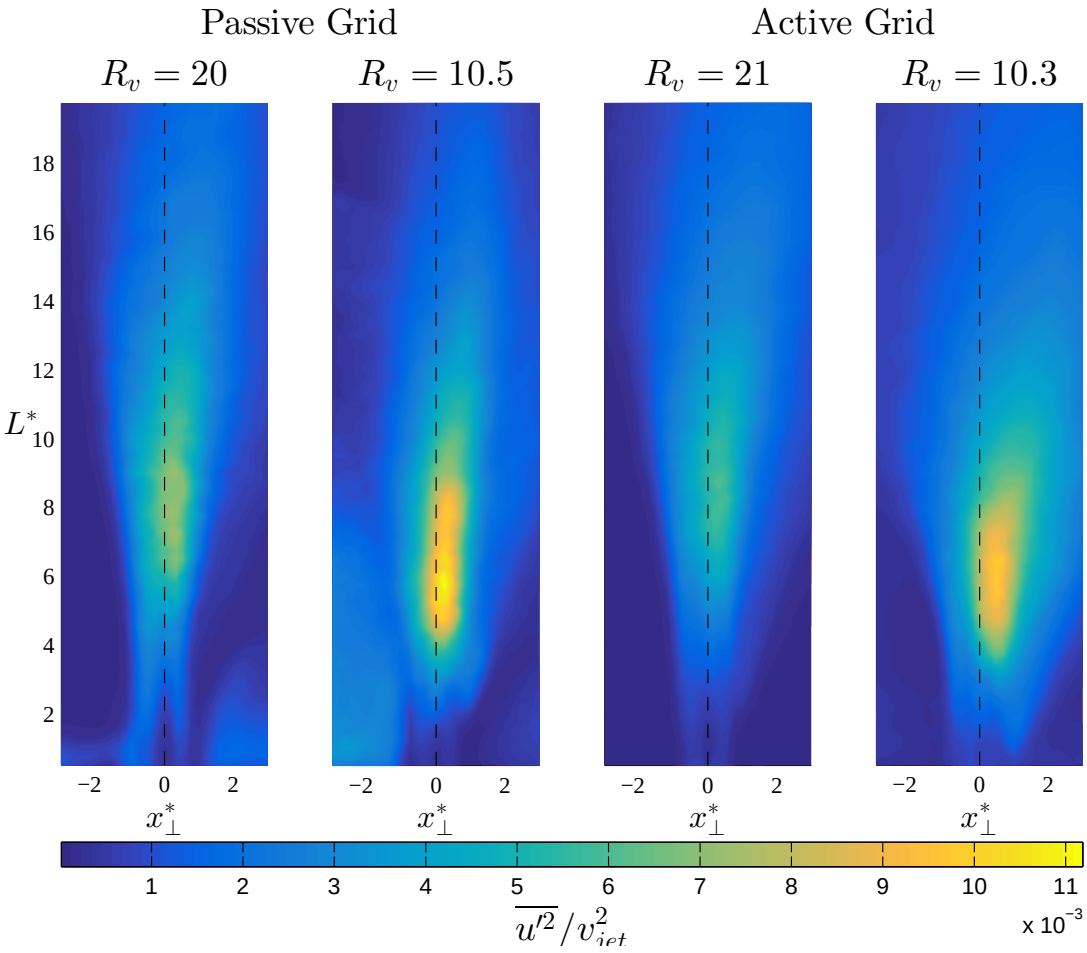

Figure 4.14: Passive grid (left two ratios) and active grid (right two ratios) contour plots of Reynolds stress component $\overline{u'u'}$

The $\overline{v'v'}$ Reynolds stress component correlates with the generation of vertical turbulence within the plume. Similar to the profile of perpendicular flow, the vertical normal stress shows the decay of the plume as it develops in the bending regime. Within the center of the plume, near the exit, there is a region of low stress before a maximum stress, which is attributed to the near constant velocity of the jet. The maximum is determined to be the beginning of the bending plume regime as the vertical velocity

component begins to decrease at a rapid rate. As the plume bends, the fluctuations in the vertical velocity decrease, and when combined with the stress profile $\overline{u'u'}$, the description of transferred momentum from $\overline{V}$ to $\overline{U}$ is expanded.

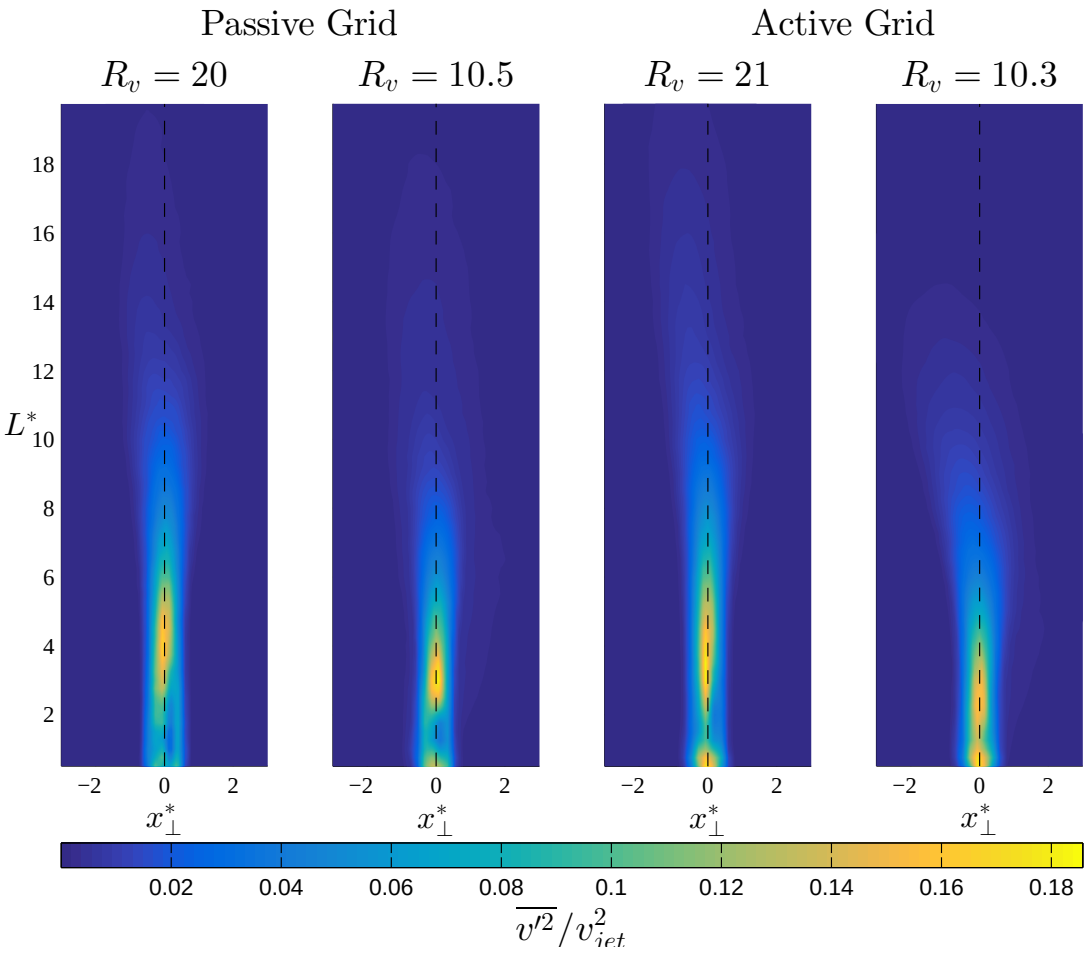

Figure 4.15: Passive grid (left two ratios) and active grid (right two ratios) contour plots of Reynolds stress component $\overline{v'v'}$

The distribution of shear stress, $\overline{u'v'}$, show the fundamental changes at the edges of the plume. Upstream and downstream of the plume, there are large regions of high stress on either side of the centerline of the plume. The sign of the stresses also in-

dicate that the free-stream flow is mixing into the plume. Positive $\overline{u'v'}$ upstream of the plume describes the free-stream flow entering the plume and negative $\overline{u'v'}$ downstream describes the fluid being pulled back into the plume. This shear stress component demonstrates the development of turbulence within the shear layer of the plume, where the the Corrsin superlayer is located. The absence of shear stress within the ambient flow, combined with the profile of the stress at any location L^* will define the superlayer both and downstream of the jet.

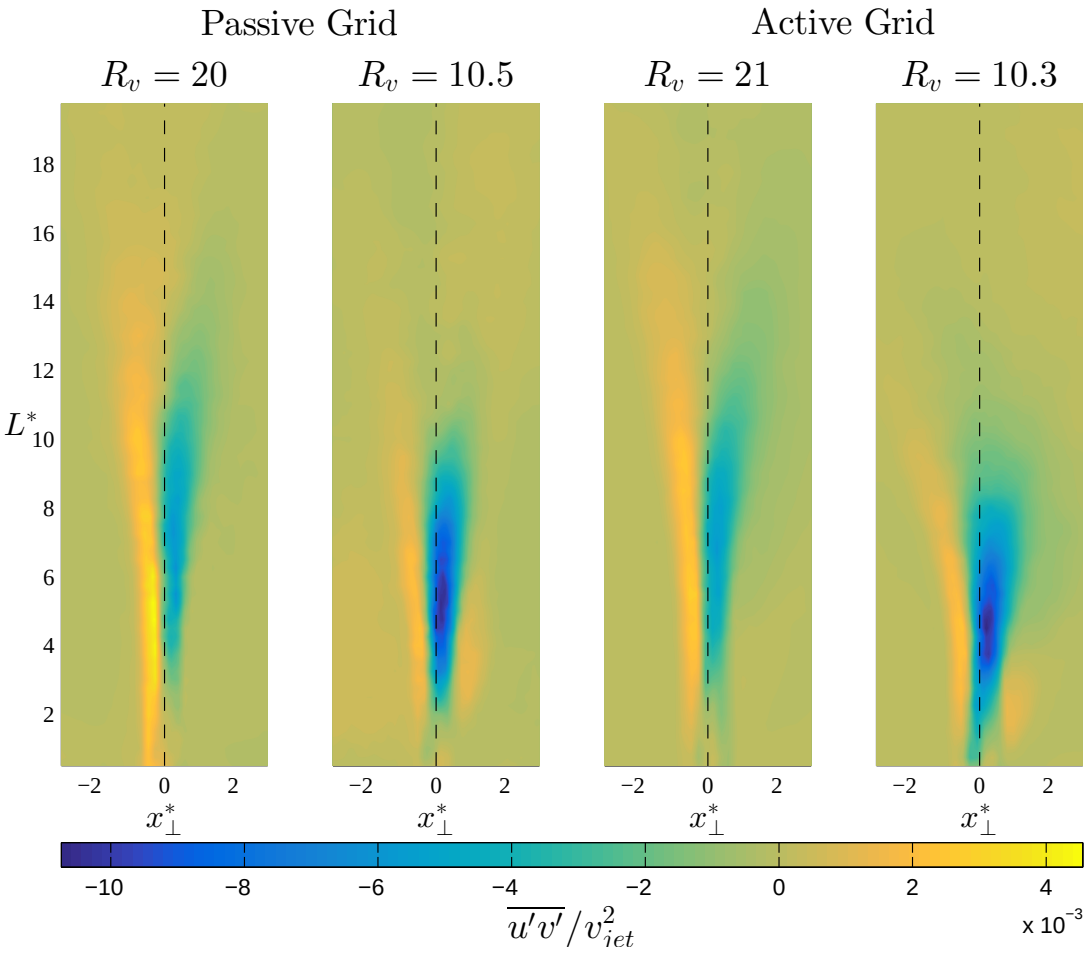

Figure 4.16: Passive grid (left two ratios) and active grid (right two ratios) contour plots of Reynolds stress component $\overline{u'v'}$

As the jet develops, the shear stresses decrease until becoming negligible. The dissipation of $\overline{u'v'}$ is influenced by the cross-flow speed. As R_v decreases, the shear stresses are larger in magnitude but become negligible earlier, shifting from $L^* \approx 16D$ to $10D$ as R_v is reduced by half.

Finally, the turbulent kinetic energy is presented to show the generation of turbulence along the plume (Figure 4.17). As the plume develops, a large region of high turbulence is found within the plume similar to the $\overline{v'v'}$ component. As the plume develops, this turbulence decreases until, at the edge of the plume, the turbulence within the plume decreases, becoming more uniform with the flow. This means that within the plume, there is a large generation of turbulence until the cross-flow becomes dominant, where the turbulence mixes with the cross-flow.

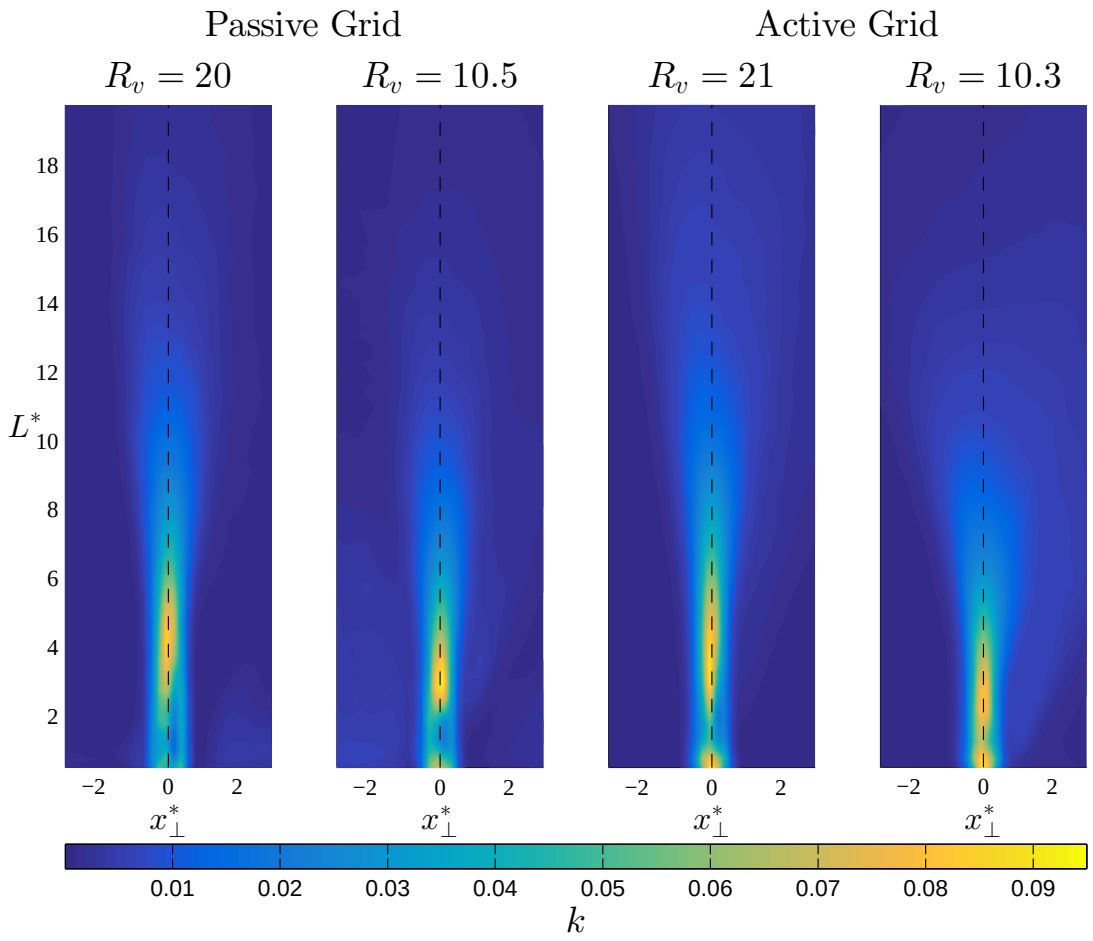

Figure 4.17: Passive grid (left two ratios) and active grid (right two ratios) contour plots of turbulent kinetic energy, k

While the velocity profiles give us an understanding of the development of the plume itself, the Reynolds stresses and turbulent kinetic energy describe the underlying influence of the free-stream flow on the plume.

Chapter 5

Discussion

5.1 Velocity field

From the results obtained from the PIV velocity field, a general characterization of the underlying flow properties of a jet in cross flow is described. The $\bar{V}$ component (Figure 4.3) presented the decay of the jet as it moved vertically in the window, dropping to 25% the initial exit velocity, as well as the growing low components downstream as the cross-flow interacts with the plume. When combined with the $\bar{U}$ and $\bar{W}$ components, the area of upstream flow movement downstream of the jet is identified as an eddy, with recirculating cross-flow moving back into the plume of equal and opposite magnitude as the cross-flow. Within the plume, the decay of the $\bar{V}$ component and the growth of the $\bar{U}$ illustrate the transfer of momentum from the cross-flow as the high jet velocity created a region of the maximum $\bar{U}$ velocity after the transition point to bending plume. The shear layer is identified as the boundary of the jet's high magnitude region and the upstream movement of ambient fluid. This boundary was found to move downward (from $\approx 14D$ to $\approx 11D$) as the ratio was decreased, highlighting the increased bending of the jet.

Introducing the Reynolds stresses and turbulent kinetic energy, the generation of

turbulence was found to exist within the plume itself and spread downstream as the cross-flow influenced its growth. A transition point was identified by noting the decay of the vertical stress, $\overline{v'v'}$, and the growth of the axial stress $\overline{u'u'}$. This location was identified by a location of shift from maximum vertical stress to maximum axial stress, which shifted closer to the exit of the jet as the ratio was decreased (from $y^* \approx 6D$ to $4D$ as the ratio). Noting the shear stress, $\overline{u'v'}$, the edges of the plume's shear layer is identified by large magnitude regions with opposite signs and equal magnitude. As the cross-flow was increased, the peak magnitudes also increased (almost 2 fold). This insight led to further examination of the plume's within the jet.

5.2 Plume characteristics

From the velocity fields, the centerline of the plume was identified and compared across several ratios. The results revealed that as the ratio is decreased ($R_v \rightarrow 1$), the plume bends at a faster rate following a parabolic trajectory. This was confirmed by plotting the slope of the plume's trajectory while also identifying a y^* location of approaching infinite slope. This is determined to be the location of where the plume begins to bend downstream after existing in the strong plume regime.

In the hopes of identifying similarities and differences between the passive and active cases by fitting the trajectory with an equation, three important plots to describe the plume were produced. The first, Figure 4.10, presented the distinguishable difference between active and passive grid data, the influence of higher turbulence causing the plume to bend earlier. The relationship between the plume transition point and the ratio was found to have a clear relationship that allows for the transition point to be described as $x_{TP} = f(R_v, I)$.

Evaluating the coefficient and exponent of the polynomial equation fitted to each plume centerline (Figure **??**), two different observations were noted. The first is that the coefficient, A, is not only linearly related to the ratio, R_v, but that the difference between the passive and active grid is very small. This coefficient can therefore be described as some simple function, $A = f(R_v, I)$. The second observation is presented in the exponent plot, B, which identifies the exponent $1/B$ required to bend the plume at the correct rate. The important result from this plot comes from Briggs's two-thirds theorem, where the plume would theoretically evolve following Equation 2.13 with an exponent of $1/B = 1/1.5$. In this experiment, the value of B is found to be more than twice the value from theory ($B \approx 3.1 - 3.6$). This indicates that the theory describing the development of the plume is not fit to define the jets trajectory. Using the derived equations, the flow-field around the centerline are examined to effectively straighten the jet for comparison.

5.3 Straightened Plume Profiles

By straightening the jets trajectory, different effects of cross-flow are presented to understand the fundamental conditions along the plume. Computation of $V_\parallel$ and $V_\perp$ velocity components along the centerline changes the velocity field's axis to a function of plume centerline and diameters off the centerline allowing the comparison of strong plumes (without cross-flow) to bending plumes. This analysis produced several observations of the influence of cross-flow. The first is the shift of $\bar{U}$ velocity from perpendicular to the flow to parallel to flow, which occurs closer to the exit of the plume as the ratio is decreased (a shift from $L^* \approx 14D$ to $7D$ for a ratio decrease of $R_v = 20$ to 10.5).

The importance of this observation is the domain of bending plume is identified as the region from decaying $\bar{V}_{\parallel}$ along the centerline until the flow is uniform inside and outside the plume. This flow was found to decrease to approximately 25% the initial jet exit velocity.

Incorporating the $\bar{V}_{\perp}$ field, the spread of the plume is identified to note the boundary of the shear layer. This is an indicator of the region of active entrainment occurring in the plume because the center of the plume will have very small or zero perpendicular velocity components. Similar to a strong plume, the flow at the boundary of the plume will be very small and opposite in sign on either side of the plume. This is seen in Figure 4.13, with flow moving toward the centerline both up and downstream of the plume.

Outside the shear layer, the flow was found to move towards the jet (downstream for cross-flow and upstream for wake recirculation) with equal and opposite signs. The maximum was found close to the exit of the jet and shifted closer to the exit as the ratio was decreased.

The additional analysis of the Reynolds stresses and turbulent kinetic energy reveal the change in the jet's development as it bends downstream. Identifying the location of the collapse of the potential core of the jet, the maximum $\overline{v'v'}$ component was found which quickly decayed until it was negligible similar to the areas outside the jet. The start of this decay matches the start of the peak of the $\overline{u'u'}$ component within the jet, showing a shift from vertical stress to axial stress. This is determined to be the location of the shift from strong to bending plume regime.

The shear stress, $\overline{u'v'}$, detailed the development of the shear layer at the edge of the jet, as two regions of equal and opposite stress is seen within the boundary of the jet

and dissipates earlier as the ratio is increased.

Chapter 6

Conclusion

From this experiment, the influence of inflow conditions were highlighted to illustrate how jets behave. The velocity field measurements illustrated the mixing of air outside the jet is found both up and downstream of the jet, moving with equal and opposite magnitude. Downstream of the plume, the boundary of positive axial flow and negative upstream movement is identified as the shear layer of the jet downstream. This is the region of interest when discussing entrainment of ambient air into plumes. This region was found to move closer to the exit of the jet as the ratio was decreased, indicating a change in the trajectory of the jet. As the fluid exits the jet at a high speed, the cross-flow changes the location of the potential core collapse, moving closer to the exit of the jet as the ratio is decreased. This location is identifiable by the generation of vertical turbulence, $\overline{v'v'}$, which transforms into axial normal stress, $\overline{u'u}$, as the jet begins to bend. This location is tracked using a piecewise polynomial to identify the transition point, y_t^*. From this, the characterization of the jet trajectory in different velocity ratios highlights the relationship between inflow conditions and the bending of the jet. The jet is described using a polynomial fit that yields a coefficient and exponent. The coefficient is linearly related to the ratio and the exponent is found to vary within a small range of values. The trajectory of the jet identified the influence

of inflow velocity on the rate of bending within the plume. This also distinguished a difference between passive and active grid, with low turbulence intensity resulting in a smaller polynomial coefficient, or reduced rate of bending. By tracking the centerline of the jet through mean flows and Reynolds stresses, the shear layer of the jet is visible, identifying the region of entrainment of ambient fluid both up and downstream of the jet. The characteristics of a plume, from near-field shear layer development, to downstream trajectory is predicted by the inflow conditions of velocity and turbulence intensity.

Bibliography

[1] J. ANDREOPOULOS AND W. RODI, *Experimental investigation of jets in a crossflow*, 138, pp. 93–127.

[2] C. BONADONNA, J. C. PHILLIPS, AND B. F. HOUGHTON, *Modeling tephra sedimentation from a ruapehu weak plume eruption*, 110, p. B08209.

[3] C. BONADONNA, M. PISTOLESI, R. CIONI, W. DEGRUYTER, M. ELISSONDO, AND V. BAUMANN, *Dynamics of wind-affected volcanic plumes: The example of the 2011 cordón caulle eruption, chile*, 120, p. 2014JB011478.

[4] G. A. BRIGGS, *Plume rise and buoyancy effects*, pp. 327–366.

[5] ——, *A plume rise model compared with observations*, 15, pp. 433–438.

[6] ——, *Plume rise predictions*, in Lectures on Air Pollution and Environmental Impact Analyses, American Meteorological Society, pp. 59–111. DOI: 10.1007/978-1-935704-23-2_3.

[7] P. CHASSAING, J. GEORGE, A. CLARIA, AND F. SANANES, *Physical characteristics of subsonic jets in a cross-stream*, 62, pp. 41–64.

[8] S. CORRSIN AND A. L. KISTLER, *Free-stream boundaries of turbulent flows*.

[9] B. J. HILL, *Measurement of local entrainment rate in the initial region of axisymmetric turbulent air jets*, 51, pp. 773–779.

[10] D. P. HOULT, J. A. FAY, AND L. J. FORNEY, *A theory of plume rise compared with field observations*, 19, pp. 585–590.

[11] J. F. KEFFER AND W. D. BAINES, *The round turbulent jet in a cross-wind*, 15, pp. 481–496.

[12] D. LIEPMANN AND M. GHARIB, *The role of streamwise vorticity in the near-field entrainment of round jets*, 245, pp. 643–668.

[13] E. J. LIST, *Turbulent jets and plumes*, 14, pp. 189–212.

[14] R. J. MARGASON, *Fifty years of jet in cross flow research.*

[15] L. MASTIN, M. GUFFANTI, R. SERVRANCKX, P. WEBLEY, S. BARSOTTI, K. DEAN, A. DURANT, J. EWERT, A. NERI, W. ROSE, D. SCHNEIDER, L. SIEBERT, B. STUNDER, G. SWANSON, A. TUPPER, A. VOLENTIK, AND C. WAYTHOMAS, *A multidisciplinary effort to assign realistic source parameters to models of volcanic ash-cloud transport and dispersion during eruptions*, 186, pp. 10–21.

[16] B. R. MORTON, G. TAYLOR, AND J. S. TURNER, *Turbulent gravitational convection from maintained and instantaneous sources*, in Proceedings of the Royal Society of London A: Mathematical, Physical and Engineering Sciences, vol. 234, The Royal Society, pp. 1–23.

[17] Z. M. MOUSSA, J. W. TRISCHKA, AND S. ESKINAZI, *The near field in the mixing of a round jet with a cross-stream*, 80, pp. 49–80.

[18] T. H. NEW, T. T. LIM, AND S. C. LUO, *Effects of jet velocity profiles on a round jet in cross-flow*, 40, pp. 859–875.

[19] F. P. RICOU AND D. B. SPALDING, *Measurements of entrainment by axisymmetrical turbulent jets*, 11, pp. 21–32.

[20] S. A. SOLOVITZ AND L. G. MASTIN, *Experimental study of near-field air entrainment by subsonic volcanic jets*, 114.

[21] S. A. SOLOVITZ, L. G. MASTIN, AND F. SAFFARAVAL, *Experimental study of near-field entrainment of moderately overpressured jets*, 133, p. 051304.

[22] L. K. SU AND M. G. MUNGAL, *Simultaneous measurements of scalar and velocity field evolution in turbulent crossflowing jets*, 513, pp. 1–45.

[23] G. I. TAYLOR AND U.S. ATOMIC ENERGY COMMISSION., *Dynamics of a mass of hot gas rising in air*, United States. Atomic Energy Commission. MDDC ;919, Technical Information Division, Oak Ridge Operations.

[24] M. J. WOODHOUSE, A. J. HOGG, J. C. PHILLIPS, AND J. C. ROUGIER, *Uncertainty analysis of a model of wind-blown volcanic plumes*, 77.

[25] X. ZHANG AND A. F. GHONIEM, *A computational model for the rise and dispersion of wind-blown, buoyancy-driven plumes—II. linearly stratified atmosphere*, 28, pp. 3005–3018.

Appendix A

Wind Tunnel measurements

When collecting PIV data in the wind tunnel, it is important to set an optimal sampling rate to capture accurate particle movement. For the most accurate data, a particle shift of 7 pixels is desired. Prior to collecting experimental data each wind tunnel setting is calibrated using LaVision's dt-optimizer script. The optimal dt values for several wind tunnel settings were documented and 700 snapshots were collected to associate velocity and the optimal PIV sampling rate (Figure A.1).

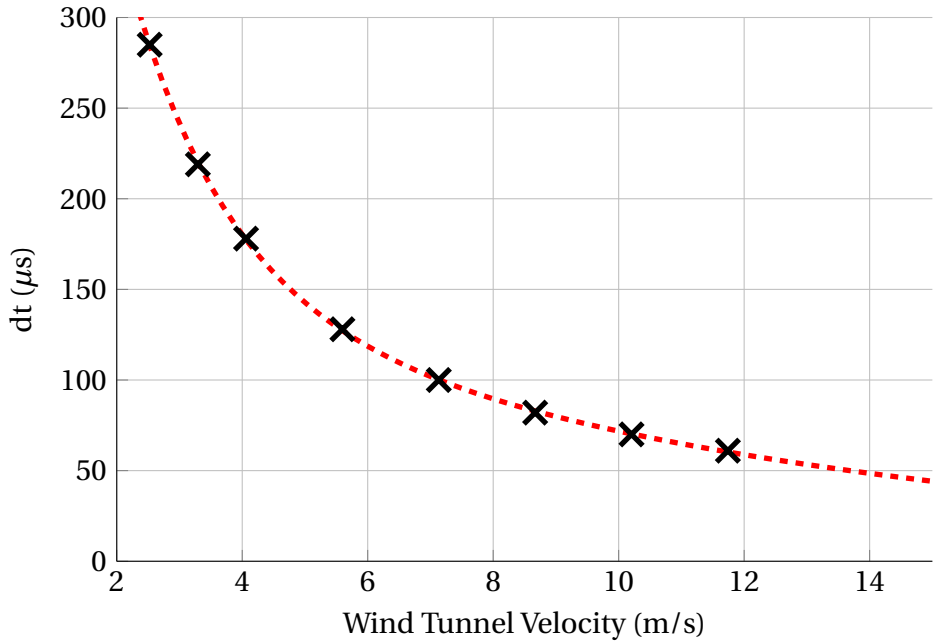

Figure A.1: Experimentally determined dt values for a seven pixel displacement in PIV

This sampling data was then used to measure the velocity of the wind tunnel at settings that were replicated in the experiments presented here. Both passive and active

grid settings are represented. The purpose of measuring the difference in wind tunnel speeds is attributed to the introduced effect of blockage in the active grid cases. This blockage results in a decrease in the mean free-stream flow while increasing the turbulence intensity which is seen in Figure A.2.

The resulting data for wind tunnel settings was found to follow a linear trend (Figure A.3) which allows for additional tests within this domain of characteristics to be conducted without additional free-stream measurements.

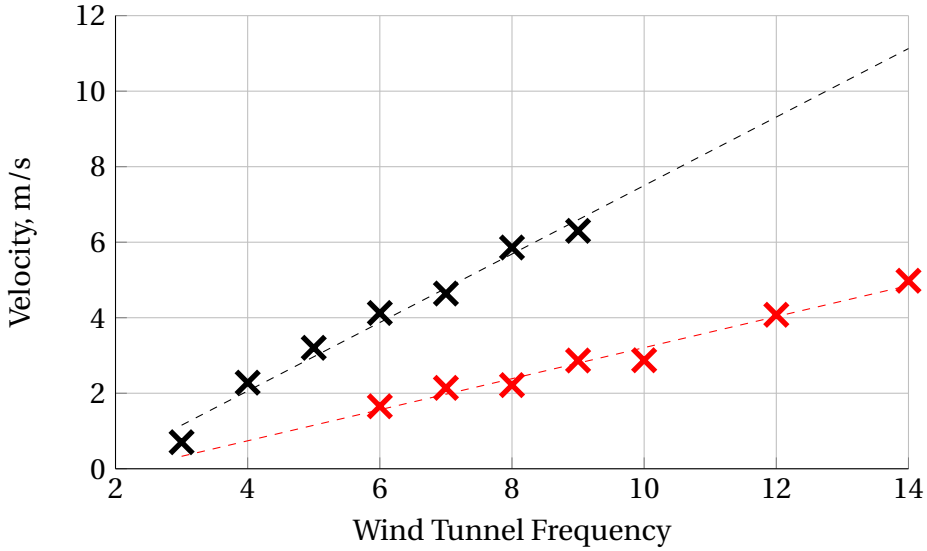

Figure A.2: Wind tunnel velocity for each corresponding protocol

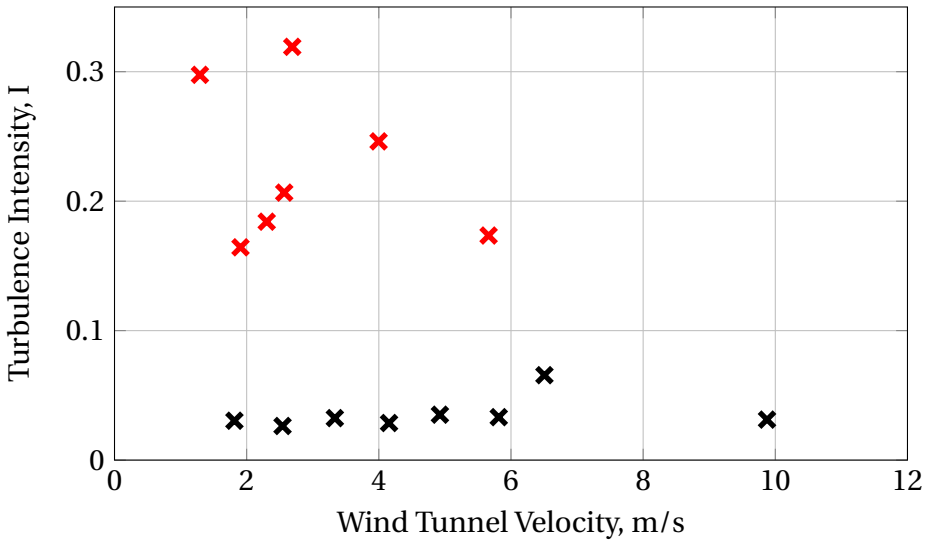

Figure A.3: Turbulence intensity measurement for free-stream flow

Appendix B

Jet Exit Location

From the raw vector field, the jet exists on an x and y axis without a clear indicator of an origin. To locate the exit of the jet, the $\bar{V}$ velocity field data was examined at the bottom of the window. For a vertical jet, a gaussian hill is expected where the center of the plume will be the maximum velocity component. As seen in Figure B.1, the data does have this characteristic, so a Gaussian fit is performed. The fit returns coefficients to satisfy the equation

$$f(x) = A \exp\left[-\left(\frac{x-B}{C}\right)^2\right], \tag{B.1}$$

where B is the center of the fit. This will provide an accurate evaluation of the centerline of the jet exit with a confidence of fit of $R^2 > 0.985$ for all cases.

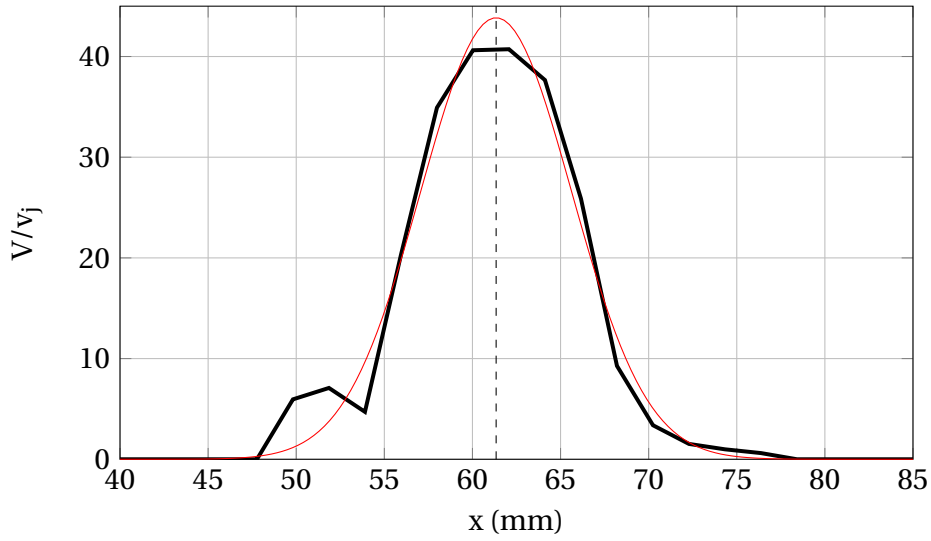

Figure B.1: Plume centerline identifier for raw $\bar{V}$ data (black) and the Gaussian fit (red)

Because several plumes were taken on the same window using the same calibration, each of those cases were analyzed and yielded the same jet exit centerline within ± 0.05 mm. For each calibration window, the centerlines were averaged to produce a mean $x^* = 0$.

Appendix C

Reynolds Averaged Navier-Stokes magnitude analysis

Using the reduced Reynolds-Averaged Navier Stokes equation with assumption made in Section 2, the individual terms are evaluated using sample data. Employing mean velocity and stress data, a surface derivative is taken using Shape-preserving piecewise cubic Hermite interpolation along either the x or y spatial coordinate. Each term is then evaluated and presented below to show dominant terms.

For the x-momentum terms (Figure C.1), all four terms contain data of the same approximate magnitude. This shows that all x-momentum interactions between the free-stream and plume are important in describing the flow. Furthermore, the resulting field can describe the development of the plume under the influence of a cross-flow.

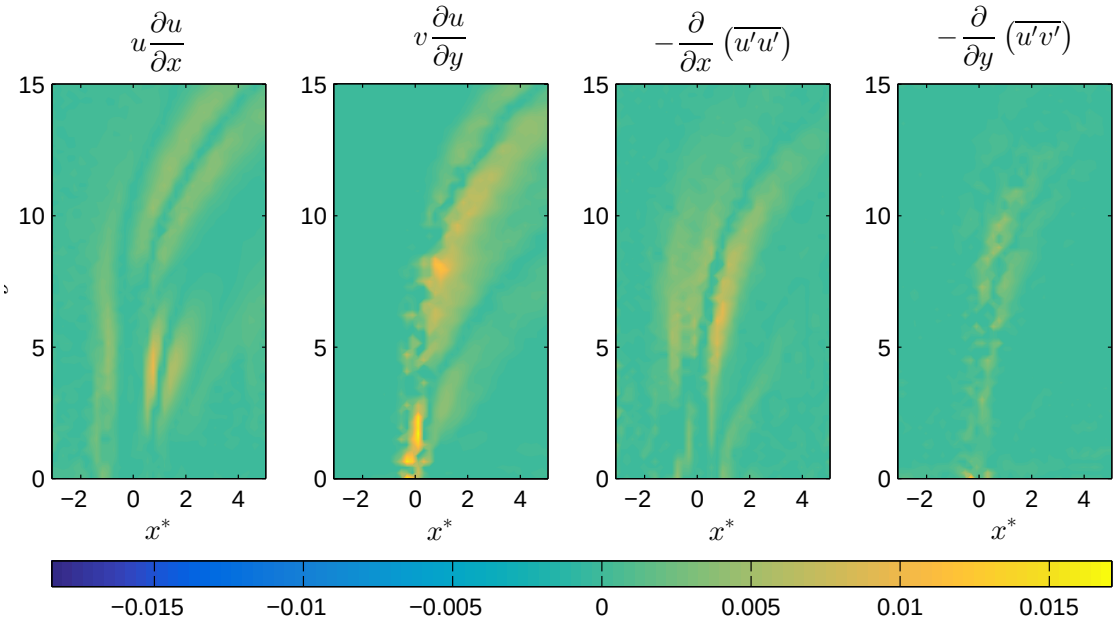

Figure C.1: Comparison of the magnitude of terms in the Reynolds Averaged Navier-Stokes x-momentum equation

For y-momentum terms, the only dominant interactions exist when describing the development of the plume, with all terms containing free-stream influence negligible to the conservation of momentum (seen as a magnitude smaller). In other words, the y-momentum described the development of the plume before it enters the bending plume domain.

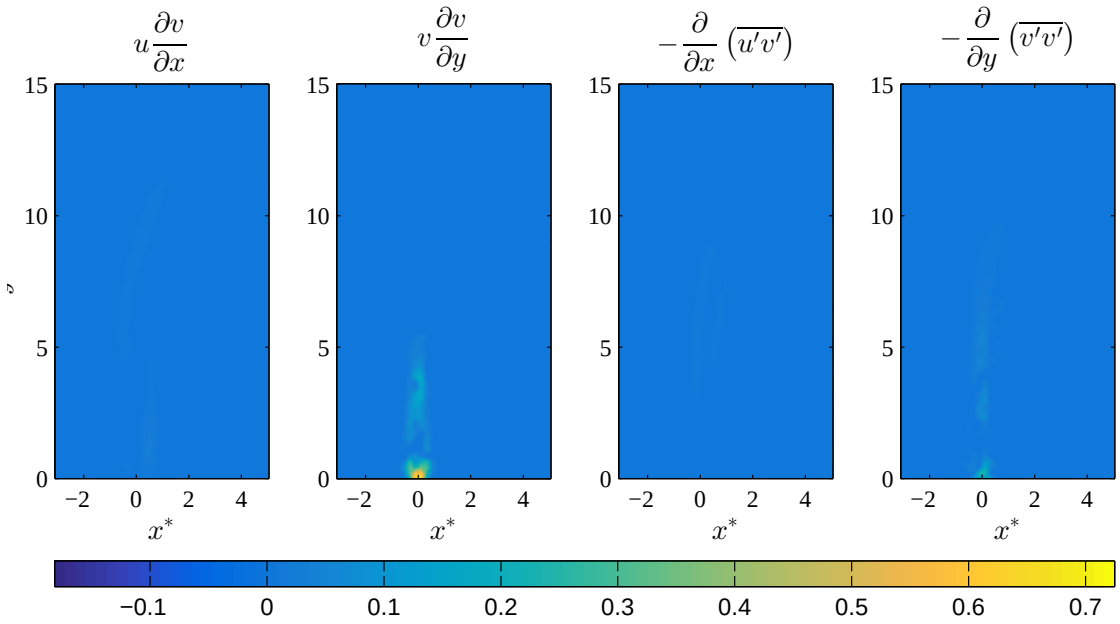

Figure C.2: Comparison of the magnitude of terms in the Reynolds Averaged Navier-Stokes y-momentum equation

The z-momentum terms are all dominant, and is noteworthy because the x derivatives highlight the activity outside the plume, while the y derivatives highlight within the plume itself.

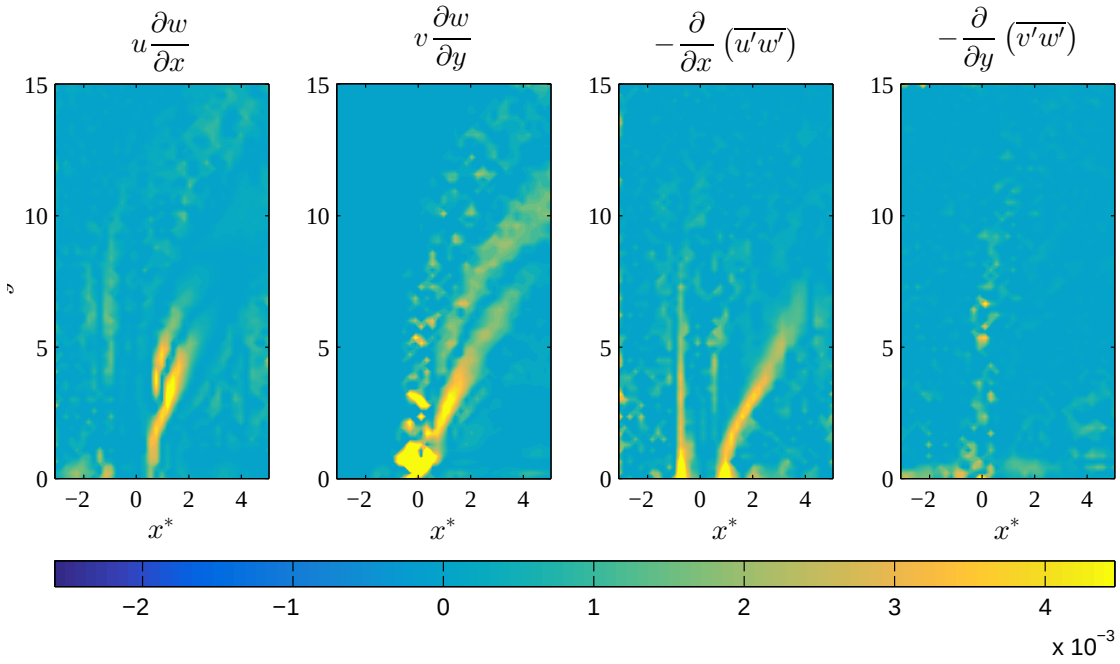

Figure C.3: Comparison of the magnitude of terms in the Reynolds Averaged Navier-Stokes z-momentum equation

Appendix D

Streamline Interpolation

In the analysis of a vector field, the streamline from any location are determined by evaluating the components at that point and mapping where a particle would move. From a two-dimensional vector field, we can trace a single particle by determining an incremental distance to be covered. If U is larger than V, this distance will be used as dx, and vice-versa if V is larger.

Choosing a starting point, (x_1, y_1), with velocity components, $\langle U_1, V_1 \rangle$, the time taken to reach the incremental distance is determined using the definition of velocity, $v = d \cdot t$. This time is then used to determine the distance traveled by the other component to give us a second point, (x_2, y_2) with velocity components $\langle U_2, V_2 \rangle$ (Figure D.1). These data points are saved along with the length of the streamline itself at any point s by defining

$$L_s = \int_0^n \sqrt{x(s)^2 + y(s)^2}\, ds \tag{D.1}$$

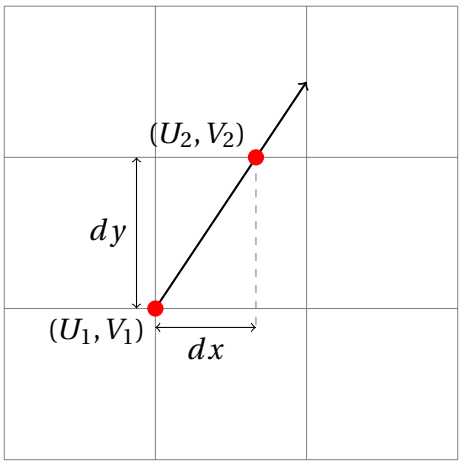

Figure D.1: Streamline interpolation method

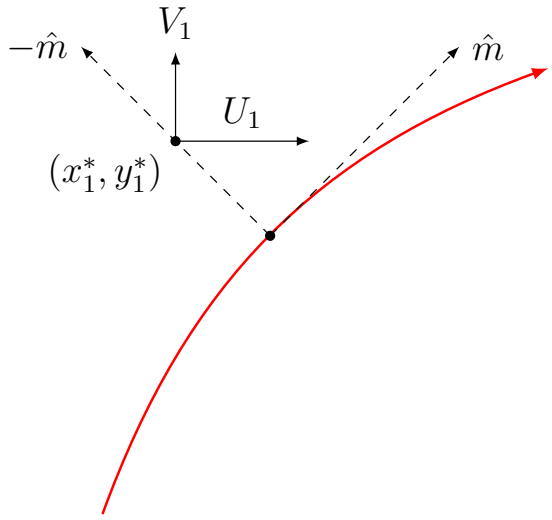

Figure D.2: Evaluation of flow-field relative to the centerline

Using the streamline data generated from the previous equation, the plume can effectively be straightened to allow for comparison between two different velocity ratios. The centerline of the plume is analyzed as a function of plume length, S_{CL}, and the length along the centerline is written in the non-dimensional form L/D, represented as L^* to describe S_{CL} in diameters from the exit.

$$L^* = \sum_{i=1}^{n} \mathrm{d}L_i^* \tag{D.2}$$

and points are chosen along the line (at intervals of $\mathrm{d}L = 0.25$) to have identical length axes. From the length location, $x^*$and y^* locations are identified on the velocity field, as well as the slope of the centerline at that location

The slope of the centerline is defined as the unit vector $\hat{m}$ (Figure D.2). The negative of the slope is the line perpendicular to the centerline and spatial coordinates are chosen at intervals of $1/3D$ from $-3D$ to $3D$ off the centerline. The velocity field data off the centerline, U and V is found using 2D interpolation of the mean velocity components and Reynolds stresses.

The velocity component moving parallel the centerline are found by evaluating the dot product of the components of the velocity,

$$V_{\parallel} = V_j \cdot \hat{m} \tag{D.3}$$

where

$$V_j = U\hat{\imath} + V\hat{\jmath} \qquad \text{and} \qquad \hat{m} = \frac{1\hat{\imath} + m\hat{\jmath}}{\sqrt{1+m^2}}$$

The flow moving parallel to the plume is defined as

$$V_{\parallel} = \frac{U + mV}{\sqrt{1+m^2}} \tag{D.4}$$

Similarly, the velocity moving orthogonally to the centerline, $V_{\perp}$, is the negative reciprocal of the slope, m, and is defined as

$$V_{\perp} = \frac{U - {}^{V}/_{m}}{\sqrt{1+\frac{1}{m^2}}} \tag{D.5}$$